

# Anisotropy and multifractal analysis of turbulent velocity and temperature in the roughness sublayer of a forested canopy

Soumak Bhattacharjee,<sup>1,\*</sup> Rahul Pandit,<sup>2</sup> Timo Vesala,<sup>3,4</sup>  
Ivan Mammarella,<sup>4</sup> Gabriel Katul,<sup>5</sup> and Ganapati Sahoo<sup>4,6,†</sup>

<sup>1</sup>*Department of Physics, Indian Institute of Science, Bangalore 560012, India.*

<sup>2</sup>*Centre for Condensed Matter Theory, Department of Physics,  
Indian Institute of Science, Bangalore 560012, India.*

<sup>3</sup>*Institute for Atmospheric and Earth System Research/Forest Sciences,  
Faculty of Agriculture and Forestry, University of Helsinki, Finland.*

<sup>4</sup>*Institute for Atmospheric and Earth System Research/Physics,  
Faculty of Science, University of Helsinki, Finland.*

<sup>5</sup>*Nicholas School of the Environment, Duke University, Durham, NC, USA.*

<sup>6</sup>*Department of Mathematics and Statistics, Faculty of Science, University of Helsinki, Finland.*

Anisotropy and multifractality in velocity and temperature time series sampled at multiple heights in the roughness sublayer (RSL) over a boreal mixed-coniferous forest are reported. In particular, a turbulent-stress invariant analysis along with a scalewise version of it are conducted to elucidate the nature of relaxation of large-scale anisotropy to quasi-isotropic states at small scales. As the return to isotropy is linked to nonlinear interactions and correlations between different fluctuating velocity components across scales, we study the velocity and temperature time series by using multifractal detrended fluctuation analysis and multiscale multifractal analysis to assess the effects of thermal stratification and surface roughness on turbulence in the RSL. The findings are compared so as to quantify the anisotropy and multifractality ubiquitous to RSL turbulent flow. As we go up in the RSL, (a) the length scale at which return to isotropy commences increases because of the weakening of the surface effects and (b) the largest scales become increasingly anisotropic. The anisotropy in multifractal exponents for the velocity fluctuations is diminished when we use the extended-self-similarity procedure to extract the multifractal-exponent ratios.

## I. INTRODUCTION

The characterization of the statistical properties of boundary-layer turbulence continues to be a challenging problem in a variety of areas including geophysical fluid dynamics and micro-meteorology. Atmospheric boundary layers provide natural laboratories for such characterization at high Reynolds number that remain outside the reach of direct numerical simulations and laboratory experiments. Because of the high Reynolds number expected, the statistical properties of the flow depend, to some extent, on the surface topography [1–3], vegetation cover [4], and thermal stratification [5]. Boundary layers over sand grains [6, 7] can be different from those above forested canopies [4, 7] in numerous ways that remain to be uncovered. It is important to understand such differences because they have a bearing on diverse applications in a variety of areas including wind-energy production [8, 9], air-pollution control [10], meteorological research [11], civil engineering [12], and ecological applications dealing with pollen and seed spread [13].

One area where atmospheric flows are contributing to a fundamental understanding of turbulence is flow near roughness elements (hereafter labelled the roughness sublayer or RSL), especially forests. The reason flow in the RSL over forests can enlighten basic turbulence research

is the scale separation characterizing the spectrum of eddies. Atmospheric boundary layers over forests are characterized by (i) large boundary depth (exceeding 1000 m), (ii) canopy heights that readily exceed 10 m, (iii) Kolmogorov dissipation length scales that are smaller than 1 mm. Another aspect of RSL flows that can be interrogated is thermal stratification. Turbulence in the RSL involves the interaction between mechanical generation of turbulent kinetic energy (TKE) and buoyancy forces that can produce or dissipate TKE. Hence, the role of thermal stratification cannot be ignored when analyzing the structure of turbulence in the RSL.

It is known that the co-spectrum of the vertical velocity and the air temperature is finite in the inertial subrange and exhibits a  $-7/3$  scaling range, suggesting that a finite interaction must exist between velocity and temperature at inertial scales, contrary to expectations based on isotropic turbulence. This finite co-spectrum is primarily because of finite mean temperature gradients. Likewise, a finite co-spectrum of vertical and longitudinal velocity components, because of finite mean velocity gradients, implies a sustained interaction between the vertical velocity and longitudinal velocities, within the inertial subrange, contrary to expectations from isotropic turbulence.

It is also well established that ramp-cliff patterns lead to dissimilarity in the multifractal properties of temperature (or any scalar) and the velocity [14, 15]; we refer the reader to Ref. [16] for a comprehensive review on ramp-cliff patterns in laboratory and field experiments, under

\* soumakb@iisc.ac.in

† ganapati.sahoo@gmail.com

different surface-roughness conditions.

Return to isotropy, with decreasing length scales, deals primarily with energy redistribution, among velocity components, and the destruction of turbulent stress. Hence, return to isotropy has been studied by using second-order statistics. Mindful of these findings and scalewise interactions between vertical velocity, temperature, and longitudinal velocity, we seek to examine to what extent scalewise return to isotropy, characterized by using the two-point measures discussed below, is retarded by (a) excess intermittency in the temperature or (b) multifractality in high-order velocity structure functions. The focus of our study is on production-to-inertial length scales, which is where the signature of TKE production and its relaxation to isotropy are most apparent.

We carry out a detailed investigation of the statistical properties of velocities and air temperatures at two different heights in the RSL above the Hyytiälä forest in Southern Finland. The statistical properties considered are (a) energy spectra, (b) second-order velocity structure functions, (c) measures of flow anisotropy that use invariant analysis [17] in the anisotropy-invariant-map (AIM) and the barycentric-map (BAM) frameworks [18], and (d) multifractal detrended fluctuation analysis (MFDFA), multifractal spectra, and multiscale multifractal analysis (MMA) for the temperature and velocity fields. These properties are all examined for different atmospheric stability conditions, which are presumed to be controlled by the stability parameter  $\zeta$  (Eq. 1). These different characterization tools have not been brought to bear simultaneously on the analysis of turbulent flows in the RSL. Our overarching goal is the quantification of the effects of surface roughness and stratification on the nature of anisotropic fluctuations and multifractal correlations in such turbulent flows. By using invariant analysis and multifractal analysis, the effects of stratification on the degree and relaxation of large-scale anisotropy at different heights in the roughness sublayer above the forest cover are quantified.

The remaining part of this manuscript is organized as follows: In Sec. II, a brief description of the experiment, its location, and the setup is provided. In Sec. III, the techniques and statistical measures that are used to characterize the flow anisotropy and the multifractality of the velocity and temperature field are reviewed. In Sec. IV, the connection between the overarching goal and the application of the aforementioned methods is presented. Section V is devoted to concluding remarks about the significance of the results for future models of the RSL.

## II. EXPERIMENTS

### A. Research site and measurements

The data sets were collected at the SMEAR (Station for Measuring Ecosystem-Atmosphere Relations) - II station located within the Hyytiälä forest in Southern Fin-

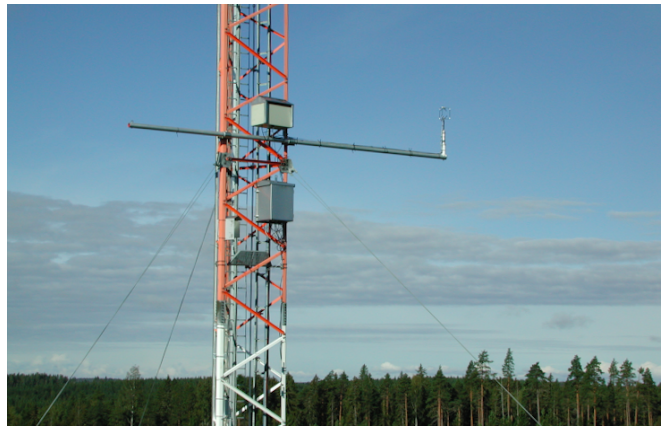


FIG. 1. The eddy-covariance tower in Hyytiälä forest. This tower is equipped with three-dimensional (3D) sonic anemometers that measure all velocity components and air temperature at high frequency (10 Hz).

land ( $61^{\circ}51' \text{ N}$ ,  $24^{\circ}17' \text{ E}$  – 180 m above sea level). The station is equipped with a tall meteorological tower where turbulence statistics are collected as part of a long-term monitoring initiative. In our study, we focus on data sampled at two heights (23.3 m and 33.0 m above ground level) in the RSL, roughly 4 m and 14 m above the canopy top. The mean canopy height is approximately  $h_{\text{canopy}} \simeq 19 \text{ m}$ . The tower is located at the highest spot in the area (181 m above sea level). In 1962, the area was regenerated by clear-cutting and sowing Scots pine seeds. The ecosystem that the SMEAR II station is surrounded by is a typical boreal forest, which is dominantly Scots pine with some spruce and birch patches further away from the measurement tower (Fig. 1). A notable spruce forest patch is located some 180 m south of the tower.

The wind velocity components and air temperature have been measured by three-dimensional sonic anemometers from Gill Instruments Ltd. (Lymington, Hampshire, England). For the 23.3 m measurement setup, the ultrasonic anemometer model is Solent Research 1012 R2 (sampling frequency at 10.41 Hz), and for the 33.0 m set-up, a Gill HS-50 ultrasonic anemometer (sampling frequency at 10 Hz) is in use.

### B. Post-processing

The measured time series of the 3 velocity components and the air temperature are divided into non-overlapping 30-minute segments. For each 30-minute segment, the coordinate system used assumes  $u_1(=u)$ ,  $u_2(=v)$ , and  $u_3(=w)$  are the longitudinal (or streamwise), lateral (or spanwise), and vertical (or wall-normal) velocity components aligned along  $x_1$  (or  $x$ ),  $x_2$  (or  $y$ ), and  $x_3$  (or  $z$ ) with  $z=0$  being the forest floor and  $x$  aligned along the mean wind direction. Primed quantities are turbulent fluctuations around their mean state defined by time-averaging over 30 minutes. Throughout, overline represents time-

averaged quantities. A standard double rotation was performed to align the velocity vector along the mean-flow direction resulting in  $\bar{v} = \bar{w} = 0$ . For notational convenience,  $\bar{u} = U$  defines the mean longitudinal velocity. A successive-difference-based despiking scheme [19] with a threshold of 10 m/s for streamwise and spanwise components, 5 m/s for the wall-normal component of the velocity, and 5 K for the air temperature was then used to identify anomalous spikes. We have not considered segments that display more than 5% spikes in a given 30-minute.

For the invariant and multifractal analyses, we have used data from these 30-minute segments. Each of these 30-minute periods is classified as stable, unstable, or near-neutral using the atmospheric stability parameter  $\zeta$ :

$$\zeta = \frac{z - z_d}{L_{obu}}, \quad L_{obu} = -\frac{u_*^3}{\kappa g \overline{w'\theta'_v}/\bar{\theta}_v},$$

$$u_*^2 = \sqrt{(\overline{u'w'})^2 + (\overline{v'w'})^2}, \quad z_d = \frac{2}{3}h_{\text{canopy}}, \quad (1)$$

where  $L_{obu}$ ,  $u_*$ ,  $\kappa$ ,  $g$ , and  $z_d$  denote the Obukhov length, the friction velocity, the von Kármán constant, the gravitational acceleration, and the estimated zero-displacement height, respectively (Table I for details). The  $\theta'_v$  denotes the potential temperature fluctuations;  $\bar{\theta}_v$ ,  $\overline{u'w'}$ ,  $\overline{v'w'}$ ,  $\overline{w'\theta'_v}$  denote the mean virtual potential temperature, the vertical component of the turbulent fluxes of horizontal momenta and potential temperature, respectively, with temporal averaging, indicated by an overline, performed over each 30-minute period; periods with  $\zeta > 0.01$ ,  $\zeta < -0.01$  and  $|\zeta| \leq 0.01$  are classified as stable, unstable, and near-neutral, respectively. In data set presented here, there are 771, 733, and 233 30-minute periods of stable, unstable, and neutral stratification at  $z_{\text{bot}}$ ; whereas for  $z_{\text{top}}$  we have 956, 683, and 98 30-minute periods of stable, unstable and neutral stratification.

### III. METHODS

Kolmogorov's 1941 (K41) phenomenological theory [20, 21] of statistically homogeneous, isotropic turbulence (assumed for small scales) does not account for multifractality; and, of course, anisotropy in eddy sizes. The local-isotropy assumption of K41 implies that the signature of TKE generation is lost as we small length scales in the energy cascade. Furthermore, the K41 exponents for second-order structure functions are affected very marginally by (a) deviations from local isotropy and (b) multifractality. It remains open to what extent the effects of TKE generation are truly lost in the scalewise turbulent cascade of each velocity component. Mathematically, the scalewise production term of TKE can be expressed in terms of the co-spectra and is given by:  $-E_{uw}(\mathbf{k})d\bar{U}/dz + (g/T)E_{wT}(\mathbf{k})$ , where  $T$  denotes the air-temperature and  $\mathbf{k}$  denotes the wave-number. So, the strength of the mean-velocity gradient  $d\bar{U}/dz$  in

the RSL and the shape of the co-spectra of both  $E_{uw}(\mathbf{k})$  and  $E_{wT}(\mathbf{k})$ , within the inertial subrange, are likely to have an effect on the return to isotropy. Differential intermittency buildup, within the velocity components, entirely ignored by K41, can slow the relaxation to local isotropy, in the inertial range. For this reason, we first discuss the spectra, co-spectra, and second-order structure functions, prior to the scalewise return to isotropy. In the first two sub-sections, an overview of the methods, which are used to characterize the anisotropy of the flows, are described. The third sub-section features the techniques with which multifractality [21–27] is analyzed.

#### A. Invariant Analysis

The anisotropy of the Reynolds stress tensor and the asymmetric distribution of the turbulent kinetic energy among the different spatial components of the velocity can be traced to stratification and surface roughness; these issues have been explored, e.g., in Refs. [7], [28], [29]. The relaxation of anisotropy, at large scales, to quasi-isotropy, at the small scales (as hypothesized in K41), e.g., via asymmetric correlations between the pressure and the rate-of-strain tensor, remains an active research area [30, 31]. Such anisotropy can be quantified and visualized by using the turbulent-stress invariant analysis [17] and the scalewise invariant analysis of the traceless deviator of the second-order velocity structure function [7].

In this invariant analysis, the invariants of the Reynolds stress anisotropy tensor are determined from [18]

$$a_{ij} = \frac{\overline{u'_i u'_j}}{2k} - \frac{1}{3}\delta_{ij} \quad \text{and} \quad k = \frac{\overline{u'_i u'_i}}{2}. \quad (2)$$

For the scalewise invariant analysis, the traceless deviator of the velocity structure-function tensor  $D_{ij}(r) = \frac{1}{2}\overline{\delta u_i(r)\delta u_j(r)}$  is used and is given by [7]:

$$A_{ij}(r) = \frac{D_{ij}(r)}{D_{kk}(r)} - \frac{1}{3}\delta_{ij}, \quad (3)$$

where  $r$  is the separation distance (a surrogate for the eddy size) that may be inferred from Taylor's frozen turbulence hypothesis.

If the turbulence is statistically homogeneous and isotropic,  $a_{ij}$  and  $A_{ij}$  are identically zero. Therefore, any deviation from these isotropic forms for these tensors can be used to quantify the anisotropy of a turbulent flow. Indeed, such invariant analysis [18, 32] has been used extensively to describe the various limiting states in turbulent flows and the route to the relaxation towards isotropy [7, 30, 33].

The state of turbulence and the relaxation to quasi-isotropic states at small scales can be effectively visualized through the trajectories of the second and the third

TABLE I. Definitions and ensemble-averaged values across all runs and stability conditions of measured and calculated variables:  $\overline{a'b'}$  denotes covariance between variables  $a$  and  $b$ ;  $\kappa = 0.4$  and  $g = 9.8 \text{ ms}^{-2}$  denote the von Kármán and the gravitational acceleration constants, respectively;  $u_* = [\overline{u'w'^2} + \overline{v'w'^2}]^{1/4} \simeq 0.44 \text{ ms}^{-1}$  (averaged across all runs and the two heights),  $\overline{u'_i u'_i} = 2k$  are the local friction velocity and twice the turbulent kinetic energy ( $= k$ ), respectively. The ensemble-averaged values are featured only to illustrate order-of-magnitude estimates of key flow properties for the entire experiment. All calculations in the figures are based on run-to-run flow statistics.

Variable	Symbol	Units	Definition	$z_{\text{bot}} = 23.3\text{m}$	$z_{\text{top}} = 33\text{m}$
Sampling frequency	$f_s$	Hz		10.41	10
Mean velocity	$\bar{U}$	m/s		2.39	3.15
r.m.s velocity	$\bar{u}_{\text{rms}}$	m/s	$(2k/3)^{1/2}$	0.81	0.83
energy dissipation rate	$\epsilon$	$\text{m}^2/\text{s}^3$	$\bar{u}_*^3 (\kappa(z - z_d))^{-1}$	$4.24 \times 10^{-2}$	$2.16 \times 10^{-2}$
Reynolds number	Re		$4k^2(9\epsilon\nu)^{-1}$	$1.54 \times 10^6$	$6.08 \times 10^6$
K41 length scale	$\eta$	m	$(\nu^3/\epsilon)^{1/4}$	$7.91 \times 10^{-4}$	$1.02 \times 10^{-3}$
K41 time scale	$\tau_\eta$	s	$(\nu/\epsilon)^{1/2}$	$5.92 \times 10^{-2}$	$1.01 \times 10^{-1}$
Strain rate	$S(z_{\text{bot}})$	$\text{s}^{-1}$	$\bar{U}_{23}(z_{\text{bot}} - z_d)^{-1}$	0.22	
	$S(z_{\text{top}})$	$\text{s}^{-1}$	$(\bar{U}_{33} - \bar{U}_{23})(z_{\text{top}} - z_{\text{bot}})^{-1}$		$7.85 \times 10^{-2}$
Shear parameter	$S^*$		$2kS/\epsilon$	38.20	48.17
	$S_c^*$		$S\tau_\eta$	$9.84 \times 10^{-3}$	$7.52 \times 10^{-3}$
Integral length scales	$L_u$	m	$\bar{U} \int \rho_{uu}(\tau) d\tau$	33.1	60.0
	$L_v$	m	$\bar{U} \int \rho_{vv}(\tau) d\tau$	26.2	54.1
	$L_w$	m	$\bar{U} \int \rho_{ww}(\tau) d\tau$	6.74	9.54
	$L_T$	m	$\bar{U} \int \rho_{TT}(\tau) d\tau$	41.2	72.3
	$r_{\text{iso}}/L_w$		Eq. (19)	0.71	1.00
	$r_{\text{ani}}/L_w$		Eq. (20)	18.56	22.56

invariants,  $I_2$  and  $I_3$ , respectively, (first invariant  $I_1 = 0$  by construction). These are given by [33]:

$$\begin{aligned} I_1 &= \lambda_1 + \lambda_2 + \lambda_3, I_2 = \lambda_1\lambda_2 + \lambda_2\lambda_3 + \lambda_3\lambda_1, \\ I_3 &= \lambda_1\lambda_2\lambda_3; \lambda_i \geq \lambda_j, \quad i \leq j, \quad i, j = 1, 2, 3, \end{aligned} \quad (4)$$

where  $\lambda_i, i = 1, 2, 3$  are the ordered eigenvalues of the tensors mentioned above. This has been used extensively to visualize the flow anisotropy in shear and wall-bounded flows [34, 35].

### B. Anisotropy Measures

1. *BAM framework*: In the *BAM framework*, the measure of flow anisotropy  $C_{\text{iso}}$  and scalewise anisotropy  $C_{\text{iso}}(r)$  are defined from the eigenvalues  $\lambda_i, i = 1, 2, 3$ :

$$C_{\text{iso}} = 1 + 3\lambda_3, \quad C_{\text{iso}}(r) = 1 + 3\lambda_3(r). \quad (5)$$

2. *AIM framework*: In the *AIM framework*, the measure of flow anisotropy  $F$  and scalewise anisotropy  $F(r)$  are defined in terms of the invariants  $I_2, I_3$  (Eq. (4)) as follows:

$$F = 1 + 27I_3 + 9I_2, \quad F(r) = 1 + 27I_3(r) + 9I_2(r). \quad (6)$$

In the case of statistically homogeneous and isotropic turbulence [18], the eigenvalues and the invariants  $I_2$  and  $I_3$ , for  $a_{ij}$  are identically 0, so both the anisotropy measures  $C_{\text{iso}}$  and  $F$  are 1.

### C. Correlation-significance testing

Given two random variables  $A$  and  $B$ , whose normalized fluctuations are  $A_n = A'/\sigma_A$  and  $B_n = B'/\sigma_B$ , the Pearson's correlation coefficient  $\rho(A, B) = \overline{A_n B_n}$ . Given  $\rho(A, B)$ , the most conventional significance testing relies on the  $t$ -statistic

$$t(A, B) = \frac{\sqrt{n-2}}{\sqrt{1-\rho(A, B)^2}} |\rho(A, B)|, \quad (7)$$

where  $n$  is the sample size. This statistic is compared with the critical value  $t_{\alpha/2, n-2}$  of a  $t$ -distribution with a level of significance of  $\alpha/2$  and  $n-2$  degrees of freedom. Here,  $\alpha$  is the chosen significance level for this test. The variables  $A$  and  $B$  are considered statistically independent when  $t(A, B) < t_{\alpha/2, n-2}$ .

## D. Multifractal Analysis

Multifractality and multiscaling corrections to K41 scaling in turbulence were introduced by Frisch and Parisi [21–23] and studied extensively thereafter (see, e.g., Refs. [21, 24–27]) including in the atmospheric surface layer [36–38]. Since then, multifractal techniques have been used not only in turbulence (for recent trends see, e.g., Refs. [27, 39–42]), but also in diverse fields including atmospheric science [43], DNA sequencing [44], heart-rate dynamics [45, 46], cloud structure [47], economics [48], and many parts of physics (see, e.g., Refs. [49, 50]).

The multifractal analysis adopted here studies fluctuations of different non-stationary fields by using two extensions of the detrended fluctuation analysis techniques, namely, Multifractal Detrended Fluctuation Analysis (MFDFA) and Multiscale Multifractal Analysis (MMA). These techniques are briefly described. The code developed in Ref. [51] is modified and used for this purpose.

### 1. Multifractal Detrended Fluctuation Analysis (MFDFA):

The MFDFA examines the scaling properties of fluctuations of a time-series  $a_i$ ,  $i = 1, \dots, N$ , where  $N$  is, as before, the length of the time series. The time-integrated series, which is referred to as a *profile* in such analysis, is obtained from:

$$Y(i) = \sum_{k=1}^i (a_k - \langle a \rangle), \quad i = 1, \dots, N, \quad (8)$$

where  $\langle \cdot \rangle$  denotes the overall mean. The *profile* is now partitioned into  $N_s = \lfloor N/s \rfloor$  segments each of length  $s$ . To incorporate the extra floating segment at the tail of the series, if  $s$  is not a divisor of  $N$ , we perform a similar partitioning, by starting from the end of the time series; this yields  $2N_s$  bins. For each partitioned bin, we calculate the order- $m$  polynomial trend and determine the variance of the *profile* as:

$$F^2(o, s) = \frac{1}{s} \sum_{i=1}^s \left\{ Y(i + (o-1)s) - y_o^m(i) \right\}^2, \quad 1 \leq o \leq N_s, \quad (9)$$

$$F^2(o, s) = \frac{1}{s} \sum_{i=1}^s \left\{ Y(N + i - (o - N_s)s) - y_o^m(i) \right\}^2, \quad N_s + 1 \leq o \leq 2N_s,$$

where  $y_o^m$  is the order- $m$  polynomial trend for the segment indexed by  $o$ .

The order- $q$  fluctuation function  $F_q(s)$  for the scale  $s$

is the generalized mean with exponent  $q$ :

$$F_q(s) = \left[ \frac{1}{2N_s} \sum_{o=1}^{2N_s} F^2(o, s)^{q/2} \right]^{1/q}, \quad q \neq 0; \quad (10)$$

$$F_q(s) = \exp \left\{ \frac{1}{4N_s} \sum_{o=1}^{2N_s} \ln [F^2(o, s)] \right\}, \quad q = 0. \quad (11)$$

The Hurst exponent  $h(q)$  follows from the scaling form  $F_q(s) \sim s^{h(q)}$  with the variable scale  $s$ . We calculate  $h(q)$  from the (best-fit) slope of the following line in the double-log plot of  $F_q(s)$  versus  $s$ , over the entire scale range of  $s$ :

$$\ln F_q(s) = h(q) \ln s + c, \quad (12)$$

where  $c$ , the intercept, is inconsequential in the calculations below. If  $h(q)$  is independent of  $q$ , the time series is labeled as monofractal, i.e., it is characterized by a single scaling exponent;  $1 > h(q) > 0.5$  indicates a correlated time series, whereas  $h(q) < 0.5$  for an anti-correlated time series [43, 45, 52].

Given  $h(q)$ , the singularity strength or Hölder exponent  $\alpha$  and the singularity spectrum  $f(\alpha)$  can be computed by using

$$f(\alpha) = \min_q [q\alpha - \tau(q)]; \quad (13)$$

i.e.,  $f(\alpha)$  is the Legendre transform of  $\tau(q) = (qh(q) - 1)$ . The  $\alpha$  and  $f(\alpha)$  are, respectively, conjugate variables of  $q$  and  $\tau(q)$ . For the time series under consideration,  $\frac{d\tau(q)}{dq}$  exists, so Eq. (13) is equivalent to:

$$\alpha = \frac{d\tau(q)}{dq}; \quad f(\alpha) = q\alpha - \tau(q). \quad (14)$$

The multifractal spectrum describing a plot of  $f(\alpha)$  versus  $\alpha$  reflects certain roughness characteristics of the time series. The width of the multifractal spectrum,  $\alpha_{\max} - \alpha_{\min}$ , as well as that of the Hurst exponent,  $h(q_{\max}) - h(q_{\min})$ , are measures of the degree of multifractality (or deviations from monofractality).

To obtain  $F_q(s)$ , linear detrending is employed, i.e.,  $m = 1$  and correspondingly  $y_p$ s are order-1 polynomials. Although  $q$  can take any real value, in any practical calculation  $q$  must be finite and discrete; we use  $q$  from  $[-5, 5]$  in steps of 0.1. The partitioning scales  $s$  have been chosen from the geometric sequence,  $s \in \{s_j, j = 1, \dots, n_{\text{scales}}\}$  defined in Eq. (15) below [51]:

$$s_j = \left[ 2^{s_{\min} + (j-1)\delta l} \right], \quad \delta l = \frac{\log_2(s_{\max}/s_{\min})}{n_{\text{scales}} - 1}, \quad (15)$$

where  $\lfloor \cdot \rfloor$  denotes rounding to the nearest integer. We have chosen  $n_{\text{scales}} = 19$ ; the choice of scales  $s_{\min}$  and  $s_{\max}$  is dictated by (i) the limitations of the algorithm used and (ii) the physical processes of interest. The former dictates a range  $s_{\min} = 32$  and  $s_{\max} = 1024$ . For  $s > s_{19} = s_{\max} \simeq N/18$ , averages are unreliable (given

our data), whereas for  $s < s_1 = s_{\min}$ , arithmetic underflow occurs, so the values of the Hurst exponents are not reliable [43, 45, 52]. We are interested in the scaling of structure functions in the inertial range, so we use  $6 < s < 340$ . Thus, for our analysis, we choose the scales commensurate with both these criteria:  $32 < s < 340$ .

## 2. Multiscale Multifractal Analysis (MMA):

In the MMA, a scale-dependent Hurst exponent  $h(q, s)$  can be computed as [45]:

$$\ln F_q(s) = h(q, s) \ln s + c, s \in [s_{\text{low}}(s), s_{\text{high}}(s)], \quad (16)$$

over a window  $[s_{\text{low}}(s), s_{\text{high}}(s)]$ ; we choose  $s_{\text{lower}}(s_j) = s_{j-2}$  and  $s_{\text{upper}}(s_j) = s_{j+2}$  for this linear fit, so we have expanding windows  $[s_{j-2}, s_{j+2}]$ ,  $j = 3, \dots, n_{\text{scales}} - 2$ , which are required for MMA calculations [43, 45]. Here it should be noted that the scale axis in the Hurst-surface plots presented later is calibrated so as to show the beginning of the fitting windows  $\{s'_j\}$ .

For a multifractal time series,  $h(q, s)$  exhibits intricate scale-dependent properties [43]. By comparing the Hurst surfaces  $h(q, s)$  for different velocity components, the anisotropy of a turbulent flow is expanded to include scalewise measures of roughness and intermittency.

## IV. RESULTS

We first present the findings from the invariant analysis in sub-section IV A, followed by the results of the MF DFA and MMA analyses. We also discuss the key features of certain bulk and scalewise changes as well as their connections and variations with stability.

### A. Anisotropy Analysis

In Fig. 2 (a) log-log plots of the ensemble-averaged and compensated total-energy spectrum  $E(f)f^{5/3}\epsilon^{-2/3}$ ; and componentwise energy spectra (for the longitudinal, transverse, and wall-normal components)  $E_{uu}(f)f^{5/3}\epsilon^{-2/3}$ ,  $E_{vv}(f)f^{5/3}\epsilon^{-2/3}$ , and  $E_{ww}(f)f^{5/3}\epsilon^{-2/3}$  are presented, respectively, in Figs. 2 (b), (c), and (d) for  $z_{\text{bot}} = 23.3m$  (blue) and  $z_{\text{top}} = 33m$  (red). A well-developed  $-5/3$  scaling region is observed only for the longitudinal energy spectrum (in the blue shaded region).

In terms of time-scale separation, the Corrsin-Ubroi criterion is satisfied because the ratio of the Kolmogorov to the mean-shear time scale  $S_c^* = \eta/(S^{-1})^{-1} = S(\nu/\epsilon)^{1/2}$  is small (Table I); also,  $\eta^{-1} \gg k \gg (S^3\epsilon^{-1})^{1/2}$  so we can expect the flow, at small length scales, to be approaching a locally isotropic state. However, because of large mean gradients within the RSL in velocity [53] and temperature [54], the inertial-range shear-stress and

heat flux co-spectra are not zero and exhibit a  $-7/3$  scaling exponent. This is indeed the case, as shown from the compensated shear-stress co-spectra [55] in Fig. 2(e). These co-spectra exhibit well-developed  $-7/3$  scaling regimes in the wave-number range where both the longitudinal and wall-normal energy spectra exhibit power-law regions with exponents  $\simeq -5/3$ . The corresponding correlation co-spectra  $R_{uw}(f)$  (Fig. 2(f)) also show power laws with exponents  $\simeq -2/3$  (not shown). We give plots of the shear co-spectra only in the low-frequency range where the flow is anisotropic. These low frequencies are determined as less than  $f_{\text{max}}^{z_{\text{bot}}} = 0.48Hz$  and  $f_{\text{max}}^{z_{\text{top}}} = 0.52Hz$ , for  $z_{\text{bot}}$  and  $z_{\text{top}}$ , respectively. The aforementioned frequencies correspond to the length scales  $l^{z_{\text{bot}}} = 4.92m < l^{z_{\text{bot}}} = 6.03m$ , respectively, where (quasi-) isotropy is attained and experimental values occur with both signs (Fig. 2(f)). It can be surmised that small-length-scale quasi-isotropy is attained, when identified by the scaling laws, more so at  $z_{\text{top}}$ , in the RSL, than at  $z_{\text{bot}}$ . Black dotted lines, parallel to the horizontal axis are shown for reference; in Figs. 2 (e) and (f), the orange lines (dashed, for  $z_{\text{top}}$ , and dashed-dotted, for  $z_{\text{bot}}$ ) mark the commencement of the  $-7/3$  scaling regime for the shear-stress co-spectra.

With regard to temperature, Figs. 2(g) and (h) show the compensated plot of the temperature power spectra  $E_{TT}(f)f^{5/3}\epsilon^{1/3}$  and (wall-normal) velocity-temperature co-spectra  $E_{wT}(f)f^{7/3}\epsilon^{-1/3}$ , respectively. The vertical velocity-temperature co-spectra is only shown in the low-frequency range for  $f < \tilde{f}_{\text{max}}^{z_{\text{top}}} = 0.26Hz \simeq \tilde{f}_{\text{max}}^{z_{\text{bot}}} = 0.21Hz$ , respectively, beyond which experimental values occur with both signs. These frequencies  $\tilde{f}$  correspond to length scales at which the flow is anisotropic. For a detailed discussion on the other possible power-laws and the implications of these scaling exponents, we refer the reader to Ref. [56].

In Fig. 3, log-log plots of the ensemble-averaged, diagonal components of the structure functions  $D_{u_i u_i}$ ,  $(u_1, u_2, u_3) = (u, v, w)$ , normalized by  $\bar{u}_i \bar{u}_i$  against normalized scales are shown. The K41 scaling form  $r^{2/3}$  is indicated by black dashed lines in the inertial range. We do not observe a distinct logarithmic scaling [7, 57] in the longitudinal (streamwise) second-order structure function  $D_{11}$  (Fig. 3) or a  $f^{-1}$  scaling in longitudinal energy spectra  $E_{uu}$  in Fig. 2 (b) neither at  $z_{\text{bot}}$ , nor at  $z_{\text{top}}$ .

Yellow shading highlights regions where the structure functions show approximate  $r^{2/3}$  scaling; this K41-type range is smaller for the wall-normal and the transverse components than for the streamwise component. Within the roughness sublayer, the range of K41-type scaling is different at different heights and for different velocity components.

Figure 4 shows the ratios of the diagonal components of the second-order structure function. These ratios are more sensitive to anisotropy than scaling exponents in structure functions. The ratios exhibit some deviations

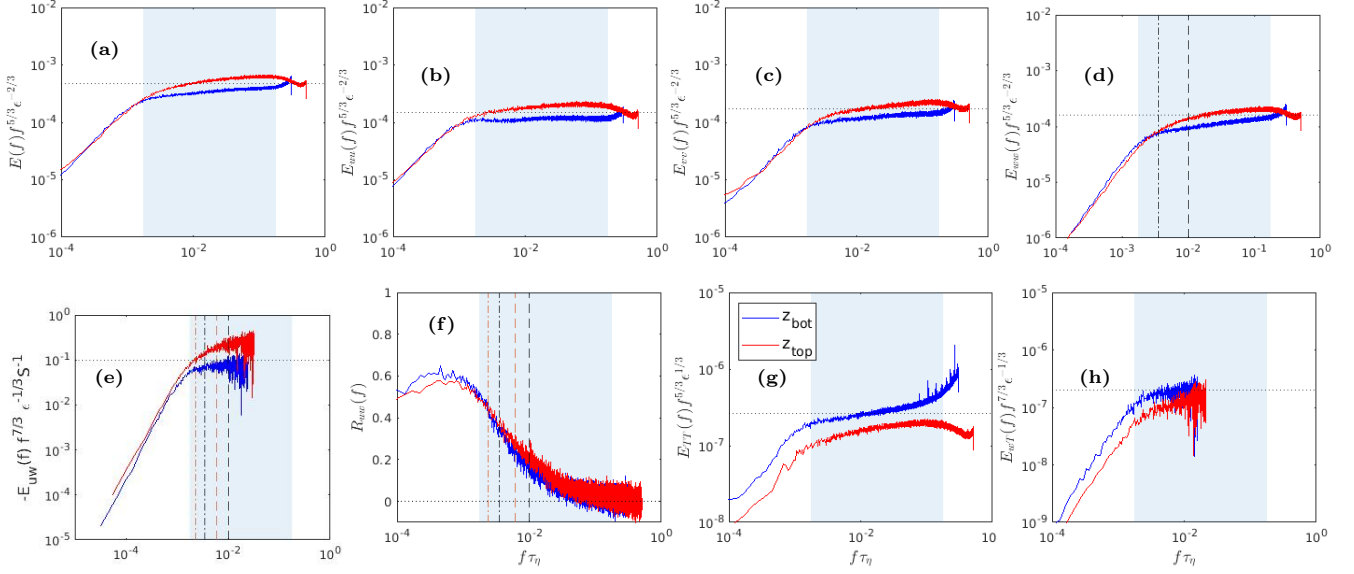


FIG. 2. Log-log plots of spectral and co-spectral variables versus the normalized frequency  $f\tau_\eta$  (with  $\tau_\eta$  the K41 dissipation time scale), of ensemble-averaged and compensated (a) total-energy spectrum  $E(f)f^{5/3}\epsilon^{-2/3}$  and componentwise energy spectra (b)  $E_{uu}(f)f^{5/3}\epsilon^{-2/3}$ , (c)  $E_{vv}(f)f^{5/3}\epsilon^{-2/3}$ , (d)  $E_{ww}(f)f^{5/3}\epsilon^{-2/3}$ , at  $z_{\text{bot}} = 23.3m$  (blue),  $z_{\text{top}} = 33m$  (red), (e) shear-stress co-spectra  $E_{uw}(f)f^{7/3}\epsilon^{-1/3}S^{-1}$ , (f) correlation co-spectra  $R_{uw}(f)$ , with a  $-2/3$  scaling (not shown), (g) compensated temperature power spectra  $E_{TT}(f)f^{5/3}\epsilon^{-1/3}$ , and (h) compensated (wall-normal) velocity-temperature co-spectra  $E_{wT}(f)f^{7/3}\epsilon^{-1/3}$ . Regions shaded in blue show the spectral range in which the energy spectrum shows an approximate  $-5/3$  scaling for the power spectra and  $-7/3$  scaling for the co-spectra. Note that (e) is shown only in the low-frequency range because, for  $f > f_{\text{max}}$  where isotropy is reached, experimental values appear with both signs. Note that  $f_{\text{max}}^{z_{\text{top}}} < f_{\text{max}}^{z_{\text{bot}}}$ . Orange lines (dashed for  $z_{\text{top}}$  and dashed dots for  $z_{\text{bot}}$ ) mark the commencement of the  $-7/3$  scaling range for the shear-stress co-spectra; and black lines (dashed for  $z_{\text{top}}$  and dashed dots for  $z_{\text{bot}}$ ) indicate the beginnings of the  $-5/3$  scaling range for the wall-normal velocity spectra. We have averaged the normalized variables over stable, unstable and near-neutral stratification for the above graphs.

from the K41 expectation (shown by black dotted lines for low turbulent intensity) for both  $z_{\text{bot}}$  (a), (c) and  $z_{\text{top}}$  (b), (d) and for different stability conditions: stable (green), unstable (red), and neutral (blue). The values in the region of a  $2/3$  scaling (highlighted in yellow) are close to the K41 result; deviation from this is significant at larger length scales (as expected). It is to be noted that for locally isotropic conditions  $D_{vv}(r)/D_{ww}(r) = 1$ , whereas  $D_{uu}(r)/D_{ww}(r) = 3/4$  although some deviations from those ratios are expected because of the use of Taylor's frozen turbulence hypothesis as discussed elsewhere [58].

$$\begin{aligned} x_{\text{BAM}} &= C_{1c}x_{1c} + C_{2c}x_{2c} + C_{3c}x_{3c}, \\ y_{\text{BAM}} &= C_{1c}y_{1c} + C_{2c}y_{2c} + C_{3c}y_{3c}; \\ C_{1c} &= \lambda_1 - \lambda_2, C_{2c} = 2(\lambda_2 - \lambda_3), C_{3c} = 1 + 3\lambda_3. \end{aligned} \quad (17)$$

In Fig. 5, the averaged relaxation-to-isotropy trajectories in the  $(-I_2, I_3)$  plane (AIM) and in the  $(x_{\text{BAM}}, y_{\text{BAM}})$  plane (BAM) from measurements along with their counterparts in the quadratic Rotta model [7] are shown. To obtain these plots, we average over initial starting points in the AIM and BAM maps for the following different stability conditions: stable (green), unstable (red), neutral (blue). Data from measurements at

different heights are also presented: dashes with a circle for  $z_{\text{bot}}$  and dashed-dotted lines for  $z_{\text{top}}$ . For all these stability conditions, the averaged relaxation-to-isotropy path occurs along the plane-strain limit, corresponding to  $I_3 = 0$  ( $x = 0$  in the AIM framework and the central dotted line in the BAM framework). That is, once trajectories intersect the plane-strain limit, they are forced to approach local isotropy along this line.

These measurements differ substantially from the prediction of the quadratic Rotta model [30], which is given as

$$\begin{aligned} \frac{dI_2}{d\tau} &= -2(B_1 - 2)I_2 + 2B_2I_3, \\ \frac{dI_3}{d\tau} &= -3(B_1 - 2)I_3 + \frac{1}{2}B_2I_2^2, \end{aligned} \quad (18)$$

where  $B_1 = 3.4$ ,  $B_2 = 3(B_1 - 2)$ . We integrate these Rotta-model ordinary differential equations (ODEs) numerically by a fourth-order Runge-Kutta scheme. Their solutions predicts axisymmetric expansion for initial conditions with  $I_3 > 0$ ; these solutions lead to the trajectories that are shown in Figs.5 (b) and (d). Some of these trajectories lie outside the AIM domain; they are not physically realisable. It is equally significant that, the return to isotropy, by this Rotta scheme in the BAM representation, favors the prolate direction when the start-



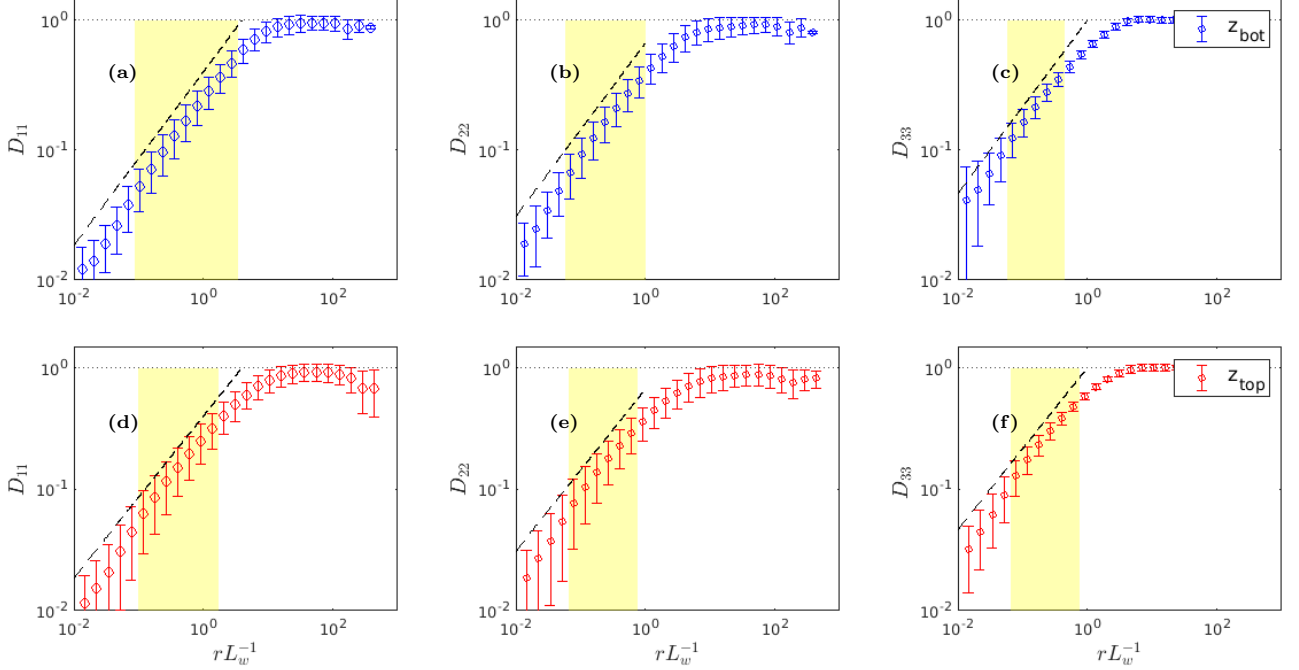


FIG. 3. Log-log plots of flow variables versus the scaled distance separation  $rL_w^{-1}$  (with  $L_w$  the integral length scale (Table I)) of the ensemble-averaged normalized structure functions  $\frac{1}{2}D_{ii}(u_i u_i)^{-1}$  (with one-standard-deviation error bars), for  $z_{\text{bot}}$  (blue) (a), (b), and (c) and  $z_{\text{top}}$  (red) (d), (e), and (f); the range of approximate  $r^{2/3}$  scaling is highlighted in yellow; the dashed line shows the K41 result, i.e., scaling with a  $2/3$  exponent.

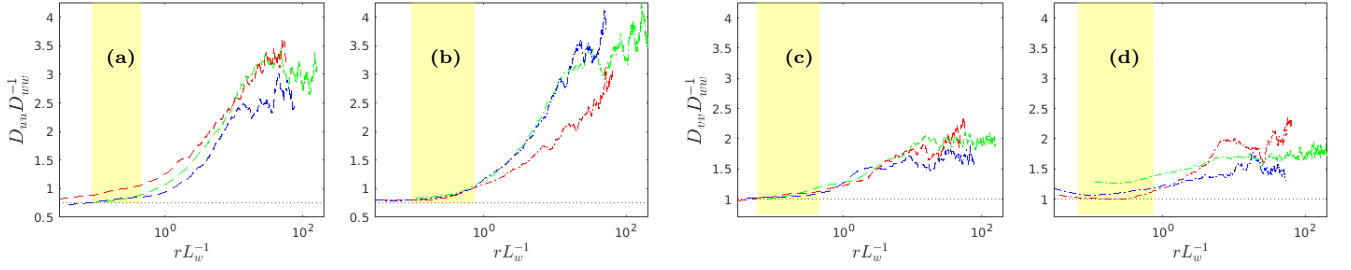


FIG. 4. Linear-log plots of flow variables versus the scaled separation  $rL_w^{-1}$  for the ratios of the diagonal components of second-order structure function; the K41 expectation is shown by the black dotted lines for  $z_{\text{bot}}$  (a and c) and  $z_{\text{top}}$  (b and d) and for different stability conditions: stable (green), unstable (red) and neutral (blue). The regions highlighted in yellow indicate where these structure functions show  $r^{2/3}$  scaling. Taylor's frozen turbulence hypothesis was used to convert time to space in both - the numerator and denominator of the abscissa. We expect some distortions due to the use of frozen turbulence; however, the normalized scale separation is likely less sensitive to those distortions.

ing trajectory is at  $x_{BAM} > 0.5$ . This return-to-isotropy trajectory, which is obtained in the Rotta scheme, is *opposite* to that in the RSL measurements, in which this trajectories is attracted to the plain-strain line.

One plausible explanation is that production terms, which are neglected in the derivation of the Rotta model, must still be active. These production terms do not favor axisymmetric expansion or a return to isotropy along the prolate side in Fig. 5 (a), (c). Therefore, we conclude that common models of scalewise return to isotropy require updating when we employ them in the RSL.

In Figs.6, linear-log plots of the isotropy measures  $C_{\text{iso}}$  (Figs.6 a and b) and  $F$  (Figs.6 c and d) are shown in the BAM and the AIM frameworks, respectively, versus the scaled separation. Data for different heights, blue for  $z_{\text{bot}}$  and red for  $z_{\text{top}}$ , are shown along with the lines  $r_{\text{iso}}L_w^{-1}$  (dashed dots) and  $r_{\text{ani}}L_w^{-1}$  (dashed) defined in Eqs. (19) and (20). Relaxation to small-scale quasi-isotropy, commences at  $r_{\text{ani}}/L_w$ , whence the anisotropy measure  $F$  increases with decreasing scales, close to the  $F \simeq 1 + 9I_2$  limit, as a consequence of the relaxation along the plain-strain limit. This relaxation concludes



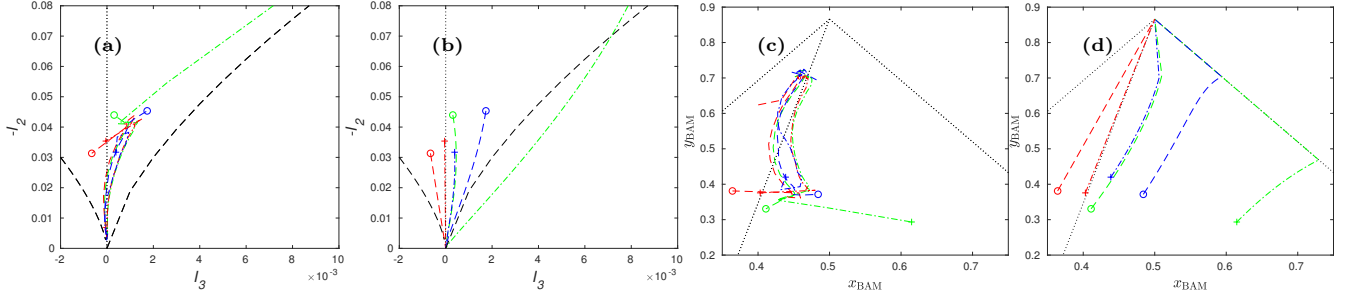


FIG. 5. Plots of the averaged relaxation-to-isotropy trajectories in the  $(-I_2, I_3)$  plane from observations (a) and (c) and those predicted (b) and (d) by the quadratic Rotta model [7]; (a) and (b) in AIM framework and (c) and (d) in BAM framework. These plots are for different stability conditions: stable (green); unstable (red); and neutral (blue); and also for different heights:  $z_{\text{bot}}$  (dashed —) with circles; and  $z_{\text{top}}$  (dashed dots —) with +.

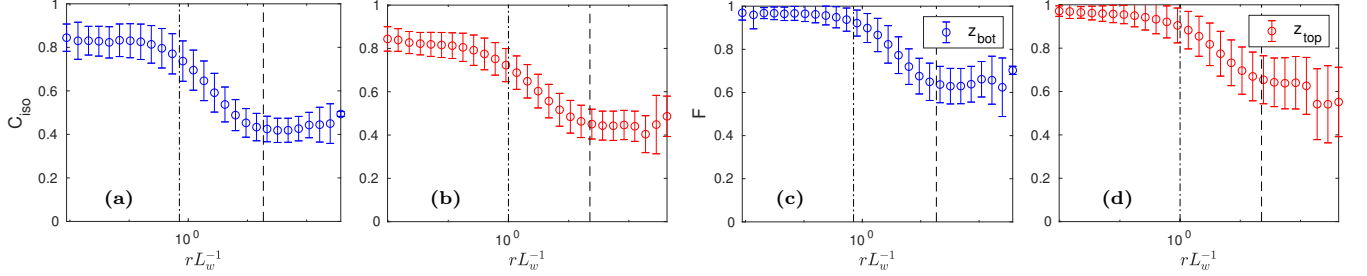


FIG. 6. Linear-log plots of the isotropy measures  $C_{\text{iso}}$  (a and b) in the BAM framework and  $F$  (c and d) in the AIM framework, versus the scaled separation, with one-standard-deviation error bars at different heights. Lines with black dash-dots indicate  $r_{\text{iso}}L_w^{-1}$ ; and the black dashed line indicate  $r_{\text{ani}}L_w^{-1}$ . Measurements at  $z_{\text{bot}}$  (a), (c) are shown in blue; whereas those at  $z_{\text{top}}$  (b), (d) are shown in red.

scales  $r_{\text{iso}}/L_w$ , given by:

$$r_{\text{iso}}/L_w = \max\{C_{\text{iso}}(r/L_w) \geq 0.9 \max\{C_{\text{iso}}\}\}; \quad (19)$$

$$r_{\text{ani}}/L_w = \min\{C_{\text{iso}}(r/L_w) < 1.1 \min\{C_{\text{iso}}\}\}. \quad (20)$$

We find that  $r_{\text{iso}}/L_w \simeq l^{\text{z}_{\text{top}}}/L_w$  for  $z_{\text{top}}$  and  $r_{\text{iso}}/L_w \simeq l^{\text{z}_{\text{bot}}}/L_w$  for  $z_{\text{bot}}$ . In the BAM measure (Fig. 6), at the smallest scales resolved,  $C_{\text{iso}}$  saturates to a value 0.8 indicating that signatures of anisotropy are still retained in the small-scale eddies. At the same time, the largest scales above the canopy top are less anisotropic, in the AIM measure, compared to higher up in the RSL. Hence, we conjecture that the interactions of the residual wakes, which originate from vegetation elements, with anisotropic attached eddies, play a role in the randomization of energies and the breakdown of eddies in the cascade.

We also explore the dependence of these characteristic scales,  $r_{\text{ani}}$  and  $r_{\text{iso}}$ , on the thermal integral length scale  $L_T$  (Table I). Such studies have been carried out in experiments above urban canopies [29] and also in the roughness and inertial sublayers [7]. In particular, we characterize the correlations between  $L_T$  and  $r_{\text{ani}}$ ,  $r_{\text{iso}}$ ,  $r_{\text{ani}}L_T^{-1}$ ,  $r_{\text{iso}}L_T^{-1}$  at  $z_{\text{top}}$  and  $z_{\text{bot}}$ , for the different stability conditions given in Table II.

The  $t$ -test in Eq. (7) is performed at a 5% significance

level (i.e.,  $t_{\alpha/2, n-2} \simeq 1.96$ .) with variables  $A$  and  $B$  set to one of the variables  $L_T$  and  $r_{\text{ani}}$ ,  $r_{\text{iso}}$ ,  $r_{\text{ani}}L_T^{-1}$ ,  $r_{\text{iso}}L_T^{-1}$ . The resulting correlation coefficients and their significance at  $z_{\text{top}}$  and  $z_{\text{bot}}$  and for the different stability conditions are presented in Table II. These correlation coefficients are small,  $< 0.2$  [7]; however, the following points can be made:

- For unstable stratification, and at both  $z_{\text{top}}$  and  $z_{\text{bot}}$ , there is significant correlation between  $r_{\text{ani}}$  and  $L_T$ , irrespective of the normalization with  $L_w$ .
- For stable stratification and unfiltered ensemble averages,  $r_{\text{ani}}$  has a significant correlation with  $L_T$ ; this is lost on normalization with  $L_w$ .
- For unstable stratification,  $r_{\text{iso}}$  is uncorrelated with  $L_T$ , irrespective of the normalization.
- For stable stratification and unfiltered, ensemble-averages, just above the canopy top (at  $z_{\text{bot}}$ ),  $r_{\text{iso}}$  is correlated with  $L_T$ , but, on normalisation with  $L_w$ , the correlation coefficients are insignificant; higher up in the roughness sublayer, we do not find conclusive evidence for such an interpretation.

We normalise the separation  $r$  by  $L_w$  because it is the most restricted length scale. Our significance tests also show that much of the dependence of  $r_{\text{ani}}$  on  $L_T$ , at both

TABLE II. Ensemble-averaged (e.a.) correlation coefficients and the test statistic  $t$  (see text) of  $L_T$  with  $r_{\text{ani}}$ ,  $r_{\text{iso}}$ ,  $r_{\text{ani}}L_T^{-1}$ ,  $r_{\text{iso}}L_T^{-1}$ , at  $z_{\text{top}}$  and  $z_{\text{bot}}$  and for the different stability conditions, stable (s) and unstable (u).

Height	Filter	$\rho(r_{\text{ani}}, L_T)$	$t(r_{\text{ani}}, L_T)$	$\rho(r_{\text{ani}}L_w^{-1}, L_T)$	$t(r_{\text{ani}}L_w^{-1}, L_T)$	$\rho(r_{\text{iso}}, L_T)$	$t(r_{\text{iso}}, L_T)$	$\rho(r_{\text{iso}}L_w^{-1}, L_T)$	$t(r_{\text{iso}}L_w^{-1}, L_T)$
$z_{\text{bot}}$	e.a.	0.160	6.75	0.035	1.44	0.110	4.60	-0.011	0.43
	s	0.146	4.08	0.033	0.91	0.187	5.28	0.046	1.27
	u	0.098	2.66	0.079	2.13	0.016	0.43	0.001	0.02
$z_{\text{top}}$	e.a.	0.167	7.05	0.016	0.68	0.019	0.80	-0.014	0.57
	s	0.183	5.73	0.008	0.24	0.048	1.49	0.001	0.03
	u	0.078	2.03	0.105	2.74	0.056	1.46	-0.044	1.14

$z_{\text{bot}}$  and  $z_{\text{top}}$  (i.e., throughout the RSL), and of  $r_{\text{iso}}$ , at  $z_{\text{bot}}$ , arises from the dependence of  $L_w$  on  $\zeta$ . In general, these results are similar to the results of measurements in the ASL and CSL [7]. For unstable stratification, however, we do not find conclusive evidence in support of such dependence.

### B. Multifractality Analysis

The results for the Hurst exponents  $h(q)$  (obtained from the MFDFA) are presented first, followed by the results for Hurst surfaces  $h(q, s)$  (obtained from MMA) based on stability. We seek to find the cause of multifractality of the temperature and velocity series. For the analysis below, only those 30-minute periods that satisfy the tests mentioned in Sec. II B are used.

In Figs. 7 (a) and (c) we plot versus  $q$  the Hurst exponents  $\bar{h}_u$ ,  $\bar{h}_v$ ,  $\bar{h}_w$ , and  $\bar{h}_T$  and the corresponding  $f(\alpha)$  spectra in Figs. 7 (b) and (d), for the original (full lines) and shuffled (dashed lines) series from the MFDFA at  $z_{\text{bot}}$  in Figs. 7 (a) and (b) and  $z_{\text{top}}$  in Figs. 7 (c) and (d).

The shuffled series are monofractal, with a  $q$ -independent Hurst exponent  $= 0.5 \pm 0.01$ , so the multifractal spectrum has a width  $\delta\alpha = \alpha_{\text{max}} - \alpha_{\text{min}}$ , which is an order of magnitude smaller than its counterpart for  $f(\alpha)$  spectra that we obtain from the original series. The corresponding Hurst surfaces for all the velocity components and temperature (not shown) are constant surfaces with  $h(q, s) = 0.5 \pm 0.01$  and contain no extra information than the corresponding Hurst exponents  $h(q)$ .

Multifractality can be traced to (1) long-range correlations or (2) a broad probability distribution function [52]. Random shuffling of a time series eliminates the long-range correlations, but it preserves the probability distribution. Thus, we can conclude that multifractality in the velocity and the temperature time series arises because of long-range correlations, which scale differently for the different velocity components and temperature. The cause of multifractality in our studies is different from that in Refs. [56, 59], where amplitude variations, studied by a telegraphic approximation [60], leads to multifractal fluctuations.

At this point, it is instructive to recall the relation of

the Hurst exponents  $h(q)$ , with the conventional, order- $p$ , multiscaling exponents that are defined via order- $p$  moments of velocity increments. We illustrate this for the velocity component  $w$ ; our discussion follows that of Meneveau and Sreenivasan (see especially pages 64-67 of Ref. [61] and Eq. (5.6)).

We begin with order- $p$  velocity structure function  $S_p^w(r) \equiv \langle |[w(\mathbf{r}_0 + \mathbf{r}) - w(\mathbf{r}_0)]|^p \rangle$ , where the angular brackets denote an average over the statistically steady state and the origin  $\mathbf{r}_0$ ; for the separation  $r = |\mathbf{r}|$  in the inertial range of scales (much larger than the dissipation scale and much smaller than the length scale at which energy is injected into the system),  $S_p^w \sim r^{\xi_p^w}$ ; this defines the order- $p$  multiscaling exponents  $\xi_p^w$ . (In homogeneous, isotropic turbulence, these exponents are defined often by using the longitudinal component of the velocity [41]). As discussed elsewhere [61], these exponents are related to the Hurst exponents as follows:

$$\xi_p = (p/3 - 1)D_{p/3} + 1; \quad (21)$$

$$\xi_p = \tau(q) + 1 = qh(q); p/3 = q; \quad (22)$$

here,  $D_{p/3}$  is the generalized dimensions and  $h(q)$  is the Hurst exponent calculated before and the superscript indicating the corresponding component has been dropped. From Eqs. (2.13, 2.14) in Ref. [61] and Eq. (14) above, it is evident that  $D_q = \tau(q)/(q - 1)$ .

In Fig. 8 we plot these order- $p$  exponents, for all the three components  $u$ ,  $v$ , and  $w$  versus  $p$  (for  $0 \leq p \leq 6$ ); we also include a plot of the K41 prediction  $\xi_p^w = p/3$  and the She-Leveque (SL) parameterization [41, 62]. The SL model is chosen because it has no tunable intermittency parameters. The error bars are large, so it is difficult to use this plot to make definitive statements about multiscaling; however, there is a systematic difference between the exponents for  $u$ ,  $v$ , and  $w$  [36, 37];  $h_w(q)$  is consistently smaller than  $h_u(q)$  and  $h_v(q)$ . We also see that  $\delta\alpha_u < \delta\alpha_v < \delta\alpha_w$ . Thus, we can conclude that the largest (smallest) is found in intermittency in the wall-normal (longitudinal) velocity components; this is consistent with the observations reported in the atmospheric surface layer [36, 37]. The anisotropy that we observe in these scaling exponents is, however, less pronounced here than in other studies over pine forests [37]; we observe  $L_u/L_w \simeq 6$  compared to  $L_u/L_w > 10$  in Ref. [37].

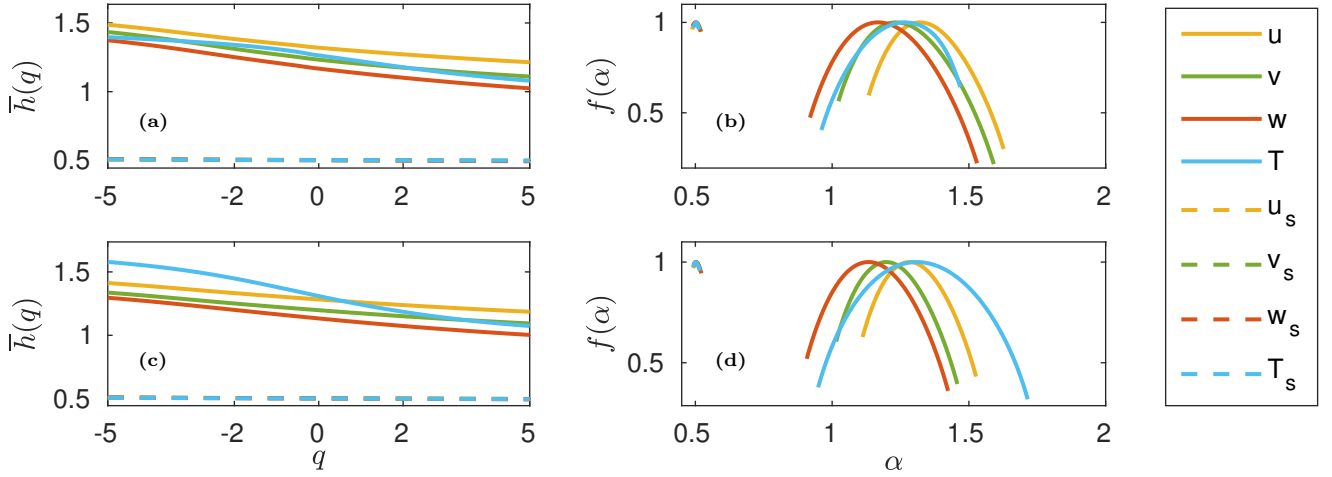


FIG. 7. Plots versus  $q$  of the Hurst exponents  $\bar{h}_u$ ,  $\bar{h}_v$ ,  $\bar{h}_w$ , and  $\bar{h}_T$  and the corresponding the  $f(\alpha)$  spectra in (b) and (d), for the original (full lines) and shuffled (dashed lines) series from the MFDFA at  $z_{\text{bot}}$  (a) and (b) and  $z_{\text{top}}$  (c) and (d). The shuffled series are monofractal with Hurst exponent  $\bar{h}(q) = 0.5 \pm 0.01$ ; correspondingly the multifractal spectrum has a width  $\delta\alpha = \alpha_{\text{max}} - \alpha_{\text{min}}$ , which is an order of magnitude smaller than its counterpart for the original series.

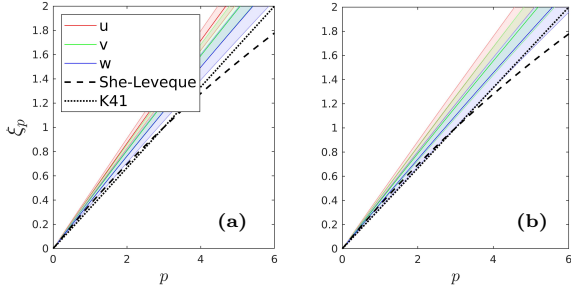


FIG. 8. Plots vs order  $p$  of multiscaling exponents  $\xi_p^{u_i}$  for different velocity components  $u$  (red),  $v$  (green),  $w$  (blue) at different heights,  $z_{\text{bot}}$  (a) and  $z_{\text{top}}$  (b), obtained from our multifractal analysis.

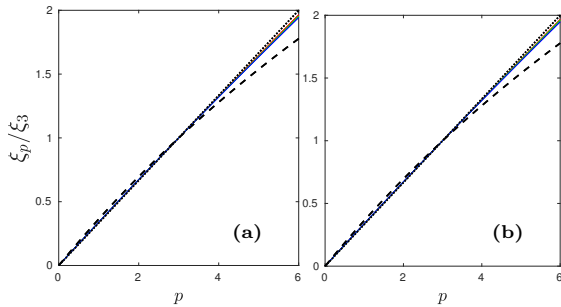


FIG. 9. Plots vs order  $p$  of ESS-normalized multiscaling exponents  $\xi_p^{u_i}/\xi_3^{u_i}$ , for different velocity components  $u$  (red),  $v$  (green),  $w$  (blue) at different heights,  $z_{\text{bot}}$  (a) and  $z_{\text{top}}$  (b), obtained from the proposed multifractal analysis here.

We find  $\alpha_0 \simeq 1.12$ , consistent with values observed in Ref. [61].

The extended-self-similarity (ESS) procedure [41, 63, 64], in which the exponent ratios, say  $\xi_p^w/\xi_3^w$ , are deter-

mined from the slopes of log-log plots of  $S_p^w$  versus  $S_3^w$  has also been used frequently to measure the scaling of these structure functions and thus to characterize multifractality [36, 37].

We have carried out the analog of this procedure by taking ratios of our Hurst exponents:

$$\xi_p^w/\xi_3^w = qh_w(q)/h_w(1), \quad p = 3q. \quad (23)$$

From these we obtain the ESS plots of the exponent ratios, which we display in Fig. 9, for  $0 \leq p \leq 6$ . As we expect from the general experience with ESS [41, 62], these exponent ratios do indicate multifractality; but the difference between the ratios for the different components,  $u$ ,  $v$ , and  $w$ , is not very striking, for low orders ( $0 \leq p \leq 6$ ); higher-order exponents require better statistics than can be obtained from the field data here. In Appendix.A, we also present the result of traditional structure function analysis. From one point measurements, it is not possible to perform the SO(3) decomposition [6, 65, 66], which can be used alternatively to calculate the anisotropic scaling of structure functions. The nature and degree of multifractality of temperature fluctuations is quite different from that of velocity fluctuations: immediately above the canopy top, temperature fluctuations are insensitive to fluctuations of small magnitudes; thus, we see a multifractal spectrum (Fig. 7 (b)) with a long left tail [51]; this is not evident higher up in the RSL, where temperature fluctuations are more multifractal (Fig. 7 (b), (d)) compared to those above the canopy.

To distinguish between different Hurst surfaces, the distance  $d_{\theta\phi}$  between the surfaces  $h_\theta$  and  $h_\phi$  for the variables  $\theta$  and  $\phi$  is used and is defined as (see, e.g.,

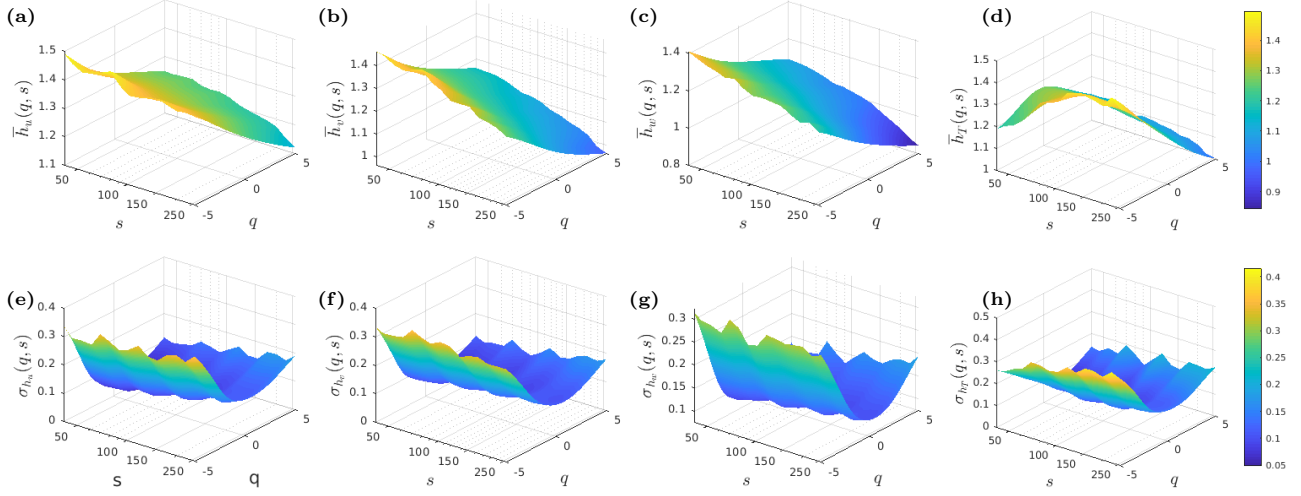


FIG. 10. Ensemble-averaged Hurst-surface plots versus  $q$  and  $s$  for (a) the longitudinal and (b) the transverse components of the velocity and (c) of the temperature; the surfaces showing the standard deviations of these surface plots are given, respectively, in (d), (e), and (f), for stable stratification and at  $z_{\text{bot}}$ . Hurst-surface plots for different stability conditions and at different heights are qualitatively similar.

Refs. [45], [43]):

$$h_{\phi^s}(q, s) = h_{\phi}(q, s) + [\langle h_{\theta}(q, s) \rangle - \langle h_{\phi}(q, s) \rangle];$$

$$d_{\theta\phi} = \{[\langle h_{\theta}(q, s) - h_{\phi^s}(q, s) \rangle^2]\}^{1/2} [\langle h_{\theta}(q, s) \rangle]^{-1}. \quad (24)$$

The variables  $\theta$  and  $\phi$  can be temperature or any one of the velocity components  $u$ ,  $v$ , or  $w$ .

In Fig. 10 representative plots are given for  $q$  and  $s$  of  $\bar{h}_u(q, s)$ ,  $\bar{h}_v(q, s)$ ,  $\bar{h}_w(q, s)$ ,  $\bar{h}_T(q, s)$  (averaged Hurst surfaces) and their standard deviations ( $\sigma_{h_u}$ ,  $\sigma_{h_v}$ ,  $\sigma_{h_w}$ ,  $\sigma_{h_T}$ ), corresponding, respectively, to streamwise, spanwise and wall-normal velocity components, and the temperature, on the scale  $s$  and for the order  $q$ .  $\bar{h}_{u_i}(q, s)$ ,  $i = 1, 2, 3$  show weak scale  $s$  dependence. Both MMA and MFDFA show interesting features for temperature-fluctuation scaling exponents,  $h_T(q)$  and  $\bar{h}_{u_i}(q, s)$  respectively; we refer the reader to Ref. [59] for other explorations.

### 1. Anisotropy in Hurst Surfaces

In Figs. 11 (a) and (b) we show, as a function of  $s$ , the cross-section of constant  $q = 1.3$  of averaged Hurst surfaces (with one-standard-deviation error bars); and in Figs. 11 (c) and (d) we show, as a function of  $q$ , the cross-section of constant  $s = 229$  of averaged Hurst surfaces (with one-standard-deviation error bars). We also show plots of  $\bar{h}_u(q, s)$  (red),  $\bar{h}_v(q, s)$  (green), and  $\bar{h}_w(q, s)$  (blue) at different heights  $z_{\text{bot}}$  (a) and (c) and  $z_{\text{top}}$  (b) and (d) for the case of stable stratification. These variations of the Hurst surfaces can be best visualized by looking at the animations that we provide in Ref. [67].

### 2. Effect of Shear on Anisotropy

TABLE III. Distance between Hurst surfaces (see text) of different velocity components along with their mean value.

$z$	$d_{vu}$	$d_{wu}$	$d_{wv}$	$\bar{h}_u$	$\bar{h}_v$	$\bar{h}_w$
$z_{\text{bot}}$	0.026	0.043	0.017	1.33	1.25	1.19
$z_{\text{top}}$	0.018	0.039	0.022	1.29	1.21	1.14

We now calculate the anisotropy in the scaling of the fluctuations of the different components of the velocity by comparing their Hurst-surface plots. For the calculations we present in this section, we have averaged over all periods, independent of stratification condition. Thus, any differences may be attributed to shear.

Table(III) summarizes the distances between the Hurst surface of the streamwise, transverse and wall-normal velocity components and the mean values of the corresponding components. We observe that  $d_{wu} > d_{vu} > d_{wv}$ , for both  $z_{\text{top}}$  and  $z_{\text{bot}}$ , but this anisotropy in the scaling of velocity fluctuations is especially evident near the canopy surface, where such distances are larger. We also calculate the componentwise distances  $d_{u_i} = d(u_i, z_{\text{top}}, u_i, z_{\text{bot}})$ ,  $i = 1, 2, 3$ :  $d_u = 0.012$ ,  $d_v = 0.020$ ,  $d_w = 0.018$ .

### 3. Effect of Stability on Anisotropy

The effect of stability is now quantified on each of the Hurst surfaces, for the longitudinal, transverse and wall-normal velocity components in Table IV. Fig. 12 (a) and

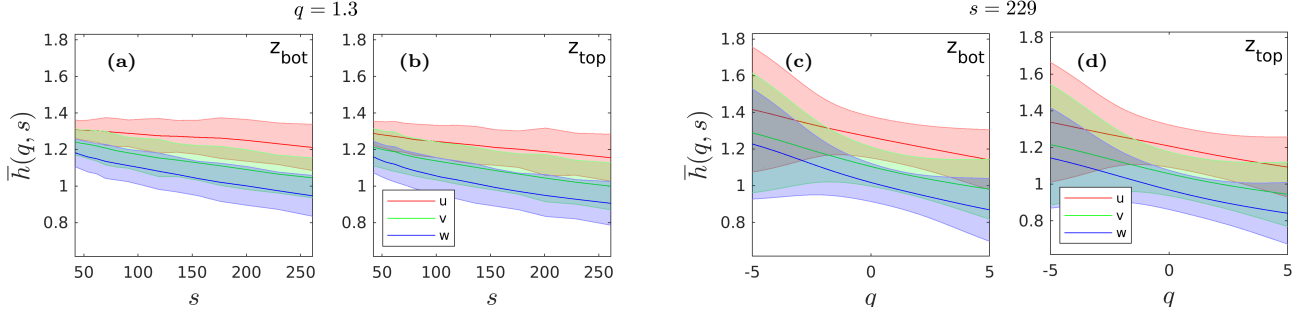


FIG. 11. Cross-sections of averaged Hurst surfaces (with one-standard-deviation error bars [68]) corresponding to different velocity components ( $\bar{h}_u(q, s)$  (red),  $\bar{h}_v(q, s)$  (green),  $\bar{h}_w(q, s)$  (blue)) for constant  $q = 1.3$  (a) and (b) and cross-sections for constant scale  $s = 229$  (c) and (d). (a) and (c) correspond to measurements at  $z_{\text{bot}}$  and (c) and (d) correspond to measurements at  $z_{\text{top}}$ . These representative plots, correspond to measurements under stable stratification ( $\zeta > 0.01$ ) and highlights the anisotropy in the scaling of velocity fluctuations.

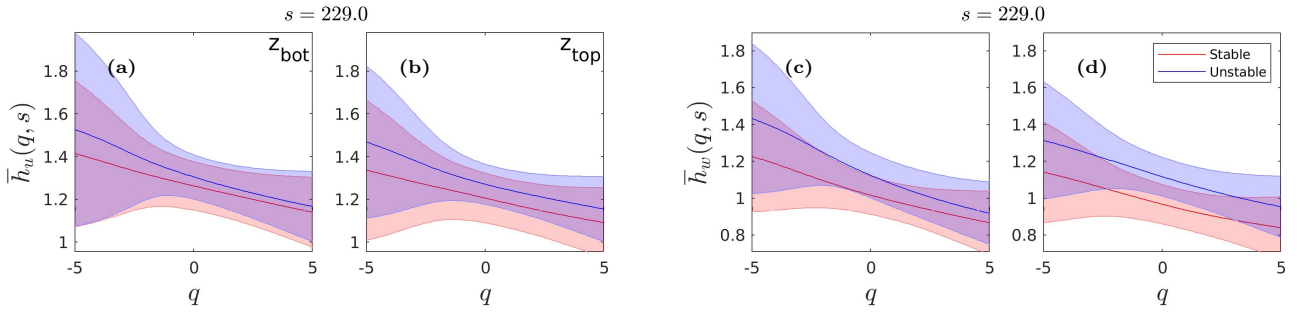


FIG. 12. Cross-sections of Hurst surfaces,  $\bar{h}_u$  (a) and (b) and  $\bar{h}_w$  (c) and (d) for scale  $s = 229$  with one-standard-deviation error bars. Hurst surfaces corresponding to stable stratification ( $\zeta > 0.01$ ) is shown in red, whereas those corresponding to unstable stratification ( $\zeta < -0.01$ ) are shown in blue; measurements at  $z_{\text{bot}}$  are shown in (a) and (c) whereas those at  $z_{\text{top}}$  are shown in (b) and (d). These are representative plots that illustrate the effect of stability on the Hurst surfaces.

TABLE IV. Distance between Hurst surfaces (see text) of corresponding velocity components for stable and unstable stratification.

Height	$d_{uu}^{\text{su}}$	$d_{vv}^{\text{su}}$	$d_{ww}^{\text{su}}$
$z_{\text{bot}}$	0.019	0.028	0.031
$z_{\text{top}}$	0.019	0.028	0.021

TABLE V. Distance between Hurst surfaces (see text) of different velocity components along with their mean values for stable and unstable stratification.

$z$	Stability	$d_{vu}$	$d_{wu}$	$d_{wv}$	$\bar{h}_u$	$\bar{h}_v$	$\bar{h}_w$
$z_{\text{bot}}$	s	0.033	0.043	0.012	1.31	1.21	1.13
	u	0.020	0.042	0.024	1.35	1.30	1.24
$z_{\text{top}}$	s	0.024	0.041	0.018	1.27	1.16	1.09
	u	0.012	0.037	0.028	1.32	1.27	1.22

(b) show the cross-sections of Hurst surfaces of the longitudinal velocity component,  $\bar{h}_u$  at  $z_{\text{bot}}$  and  $z_{\text{top}}$ , respectively, with one-standard-deviation error bars, whereas

Fig. 12 (c) and (d) show the cross-sections of Hurst surfaces of the wall-normal velocity component,  $\bar{h}_w$  at  $z_{\text{bot}}$  and  $z_{\text{top}}$ , respectively, with one-standard-deviation error bars. These cross-sections have been shown at a constant representative scale  $s = 229$ . The cross-sections of Hurst surfaces corresponding to stable stratification ( $\zeta > 0.01$ ) is shown in red, whereas those corresponding to unstable stratification ( $\zeta < -0.01$ ) are shown in blue. The correlations of multifractal fluctuations is very similar for the longitudinal and the transverse velocity components for stable and unstable stratification, compared to those for the wall-normal components. However, because of the significant overlap between the Hurst surfaces, we cannot draw any conclusive evidence.

Table V shows the effect of stability on inter-component Hurst surface distances  $d_{u_i u_j}$ .

The correlation of multifractal fluctuations for the wall-normal velocity differ significantly, for both stable and unstable stratification. With decreasing stability ( $\zeta$ ), only  $d_{vu}$  decreases, whereas  $d_{wv}$  increases, albeit marginally, throughout the RSL. Furthermore, all fluctuations show larger correlation for unstable stratification than for stable stratification.

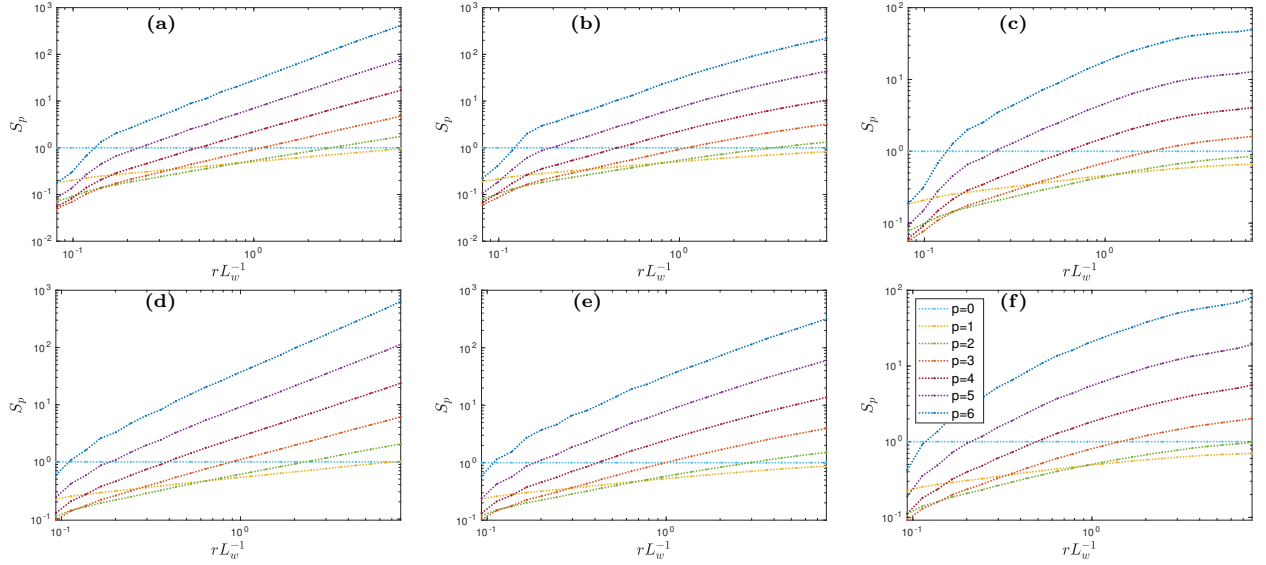


FIG. 13. Log-log plots versus the scaled separation  $rL_w^{-1}$ , of ensemble-averaged structure functions  $S_p^{u_i}$ , corresponding to the different velocity components:  $u$  (a), (d),  $v$  (b),(e), and  $w$  (c),(f) for orders  $p = 0, 1, 2, 3, 4, 5, 6$  (in cyan, yellow, green, orange, red, purple, and blue respectively) at  $z_{\text{bot}}$  (a),(b),(c) and  $z_{\text{bot}}$  (d),(e),(f).

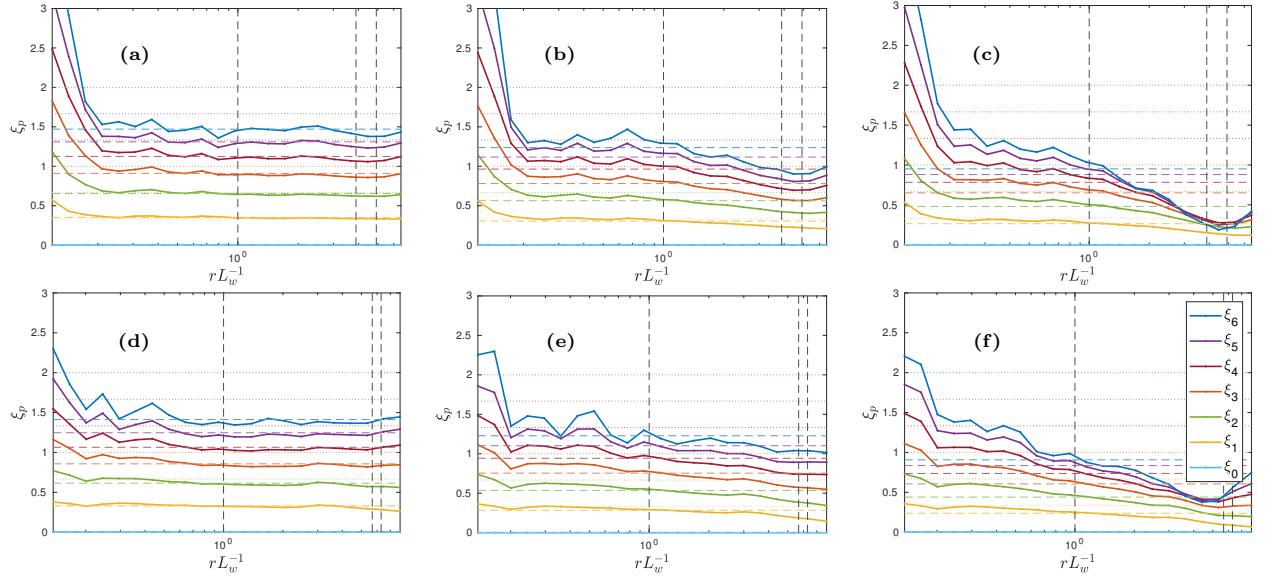


FIG. 14. Semi-log plots versus the scaled separation  $rL_w^{-1}$ , of local-slopes of ensemble-averaged structure functions  $S_p^i$  corresponding to the different velocity components:  $u$  (a),(d),  $v$  (b),(e), and  $w$  (c),(f), for orders  $p = 0, 1, 2, 3, 4, 5, 6$  (in cyan, yellow, green, orange, red, purple, and blue respectively) at  $z_{\text{bot}}$  (a),(b),(c) and  $z_{\text{bot}}$  (d),(e),(f). Horizontal dashed lines indicate the linear-regression fit (see text) and horizontal dotted line shows K41 values ( $p/3$ ); vertical-dashed lines indicate normalized (by  $L_w$ ) integral scales  $L_w, L_v, L_u$  (from left to right).

## V. DISCUSSIONS AND CONCLUSIONS

We have carried out a detailed study of the statistical properties of turbulent velocity and air-temperature in the roughness sublayer at different heights above the Hyytiälä forest. The foci of our study have been (a) anisotropy of turbulence at large scales, (b) its relaxation to isotropy at small scales, and (c) its effect on

the multiscaling exponents. This relaxation is of interest given that turbulence in the RSL exhibits multifractality in velocity and air-temperature fluctuations.

The return to isotropy commences and concludes at scales,  $r_{\text{ani}}$  and  $r_{\text{iso}}$ , respectively, that increase the higher up we go in RSL, because surface effects are weaker than they are just above the canopy. At the same time, the largest scales above the canopy top are less anisotropic,



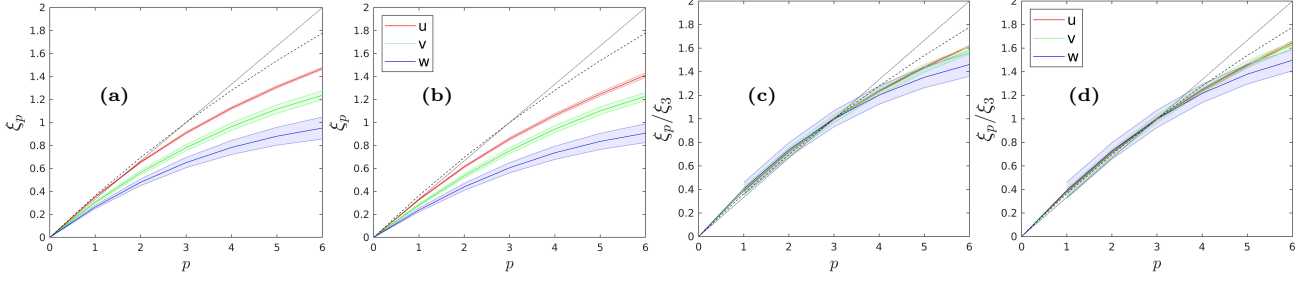


FIG. 15. Plots versus order  $p$ , of multiscaling exponents  $\xi_p^{u_i}$  (a),(b) and ESS-normalized multiscaling exponents  $\xi_p^{u_i}/\xi_3^{u_i}$  (c),(d) calculated from ensemble-averaged structure functions  $S_p^{u_i}$  using linear regression, for  $u$  (red),  $v$  (green)  $w$  (blue) versus order  $p$  along with 95% confidence intervals (shown by shaded region) from our linear regression (see text) at  $z_{\text{bot}}$  (a),(c) and  $z_{\text{top}}$  (b),(d).

in the AIM measure, compared to higher up in the RSL. This leads us to the conjecture that the interactions of the residual wakes, which originate from vegetation elements, with anisotropic attached eddies, play a role in the randomization of energies and the breakdown of eddies in the cascade.

The scale  $r_{\text{ani}}$  is smaller for stable than for unstable stratification at both heights. Both the AIM and BAM frameworks indicate that relaxation to small-scale quasi-isotropy occurs (Fig. 6); however, this return is not concluded in the BAM measure (Fig. 6), and at the smallest scales resolved,  $C_{\text{iso}}$  saturates to a value 0.8 indicating that signatures of anisotropy are still retained in the small-scale eddies. We see that the return-to-isotropy trajectories occur along the plain-strain limit, at all heights; and this similarity is most pronounced for stable stratification. By contrast, this is quite different from the predictions of the quadratic Rotta model, which predicts relaxation along the axisymmetric expansion limit.

The ensemble-averaged correlation coefficients indicate that normalized scales, at which the return to isotropy commences and concludes, are generally seen to be dependent on thermal stratification only through  $L_w$ . Whereas this is seen to be true for stable stratification, we cannot draw such a conclusion for unstable stratification, because we find  $r_{\text{ani}}$  and  $r_{\text{iso}}$  are dependent on and independent of, respectively, the thermal integral scale, irrespective of the normalization with  $L_w$ .

We find that temperature and velocity fluctuations in the inertial range display multifractality because of long-range correlations. The multifractal exponents are slightly different (although the error bars are quite large) for different velocity components; the longitudinal component being the least intermittent. The nature of multifractality differs primarily in two aspects when compared to [37]; the reduced anisotropy in multifractal exponents and the role of amplitude variability (albeit calculated by different algorithms). The multifractality of the temperature fluctuations is more than that of velocity fluctuations (Fig. 7). Immediately above the canopy top, temperature fluctuations are insensitive to fluctuations of small magnitudes; multifractality of temperature in-

creases with height in the RSL. In contrast, the multifractality of the velocity components is found to be similar above the canopy top and higher up in the RSL.

We have also looked for signatures of anisotropy in the Hurst exponents  $h(q)$  and the multiscaling exponents  $\xi_p$ , for different components of the velocity field, by using our single-point measurements. We find that the error bars for  $h(q)$  and  $\xi_p$  are large. Therefore, we have extended the scaling range by using the ESS procedure [41, 63]. This ESS procedure yields multiscaling exponent ratios  $\xi_p/\xi_3$  with smaller error bars than those we find for  $h(q)$  and  $\xi_p$ . Unfortunately, the signatures of anisotropy in  $\xi_p/\xi_3$  are much less evident than in  $\xi_p$ . An earlier study [37], with slightly different experimental conditions, has reported multiscaling exponent ratios  $\xi_p/\xi_3$  that do retain signatures of anisotropy. Improved measurements in future should allow us to use  $\xi_p$  or  $h(q)$ , without ESS, to uncover the signatures of anisotropy in these multiscaling exponents.

As we expect from field experiments, it is clearly more challenging to obtain  $h(q)$  and  $\xi_p$ , with small error bars, from measurements over forests than from laboratory experiments. We note, in passing, that the universal values of  $\xi_p$ , for statistically homogeneous and isotropic fluid turbulence, can be obtained from measurements in atmospheric boundary layers by using the  $SO(3)$  decomposition discussed in Refs. [6, 65, 66]; this is not our purpose here; but we observe that the ESS procedure, which we use here, yields exponent ratios that are not very sensitive to the anisotropy of the flow and are, therefore, very close to the universal values of these ratios for statistically homogeneous and isotropic turbulence.

We also compare the results of our MFDFA with the conventional structure-functions analysis. We find that both multiscaling exponents  $\xi_p$  and ESS multiscaling ratios  $\xi_p/\xi_3$ , obtained from structure functions, show stronger deviations from K41 compared to their MFDFA counterparts. By contrast, the anisotropy in  $\xi_p/\xi_3$  are comparable in MFDFA and the ESS procedure.

We believe that in the future, the methods developed here shall be used for the following: (a) different classes of stability, for e.g., near-neutral, mildly unstable, unsta-



ble, dynamic-convective, and free-convective, as well as stable - moderately stable, very stable with turbulence becoming patchy; and (b) different roughness configurations (say snow-no-snow, or winter vs summer - where the foliage density is quite different). It is envisaged that the methods introduced here can be used for a comprehensive characterization of anisotropy, return to isotropy, and multifractality of turbulence in the roughness sub-layer at different heights and many forest types to begin unfolding connections between distribution of foliage and turbulence in the RSL.

## ACKNOWLEDGMENTS

We thank the AtMath Collaboration at the University of Helsinki, ICOS by University of Helsinki and the DST, CSIR and KVPY (India) for support. GK acknowledges partial support from the US National Science Foundation (NSF-AGS-1644382, NSF-IOS-1754893, and NSF-AGS-2028633).

## Appendix A: Structure function scaling exponents

In Fig. 13, we show ensemble-averaged structure functions  $S_p^{u_i}$ ,  $i = 1, 2, 3$ , for  $u$  (a), (d),  $v$  (b), (e), and  $w$  (c), (f) for orders  $p = 0, 1, 2, 3, 4, 5, 6$  (in cyan, yellow, green, orange, red, purple, and blue respectively), in the inertial range. From  $S_p^{u_i}$ , we calculate the local scaling exponents (as local slopes of the structure function) shown in Fig. 14. Vertical dashed lines (from left to right) indicate the integral scales,  $L_w, L_v, L_u$ . We calculate the universal multiscaling exponents  $\xi_p^i$ ,  $i = 1, 2, 3$  from Fig. 13 by using linear-regression over the range of  $rL_w^{-1}$  that corresponds to the trough in Fig. 14. Horizontal dashed lines in Fig. 14 indicate the linear-regression fit ( $\xi_p^{u_i}$ ) and vertical-dashed lines indicate normalised integral scales  $L_w, L_v$ , and  $L_u$  (from left to right). In Fig. 15, we plot the multiscaling exponents  $\xi_p^{u_i}$  (a),(b) and ESS-normalised multiscaling exponents  $\xi_p^{u_i}$  (c),(d) versus order- $p$ . We see that the multiscaling exponents obtained from the traditional structure function analysis, indicate larger intermittency compared to MFDA; by contrast the anisotropy from both the calculations are comparable.

- 
- [1] J. Yuan and M. Aghaei Jouybari, Phys. Rev. Fluids **3**, 114603 (2018).
  - [2] B. Chen, M. Chamecki, and G. G. Katul, Quarterly Journal of the Royal Meteorological Society **145**, 2101 (2019).
  - [3] D. Poggi and G. G. Katul, Boundary-layer meteorology **129**, 25 (2008).
  - [4] M. R. Raupach and A. S. Thom, Annual Review of Fluid Mechanics **13**, 97 (1981), <https://doi.org/10.1146/annurev.fl.13.010181.000525>.
  - [5] G. G. Katul, A. G. Konings, and A. Porporato, Phys. Rev. Lett. **107**, 268502 (2011).
  - [6] S. Kurien and K. R. Sreenivasan, Phys. Rev. E **62**, 2206 (2000).
  - [7] P. Brugger, G. G. Katul, F. De Roo, K. Kröniger, E. Rotenberg, S. Rohatyn, and M. Mauder, Phys. Rev. Fluids **3**, 054608 (2018).
  - [8] B. C. Ummels, M. Gibescu, E. Pelgrum, W. L. Kling, and A. J. Brand, IEEE Transactions on Energy Conversion **22**, 44 (2007).
  - [9] J. M. Carrasco, L. G. Franquelo, J. T. Bialasiewicz, E. Galvan, R. C. PortilloGuisado, M. A. M. Prats, J. I. Leon, and N. Moreno-Alfonso, IEEE Transactions on Industrial Electronics **53** (2006), 10.1109/TIE.2006.878356.
  - [10] E. Demirci and B. Cuhadaroglu, Energy and Buildings **31**, 49 (2000).
  - [11] W. A. Tesfuhuney, S. Walker, L. D. V. Rensburg, and C. S. Everson, Atmosphere **4**, 428 (2013).
  - [12] J. E. Cermak, Journal of Wind Engineering and Industrial Aerodynamics **91**, 355 (2003).
  - [13] R. Nathan and G. G. Katul, Proceedings of the National Academy of Sciences **102**, 8251 (2005).
  - [14] K. R. Sreenivasan, R. A. Antonia, and D. Britz, Journal of Fluid Mechanics **94**, 745–775 (1979).
  - [15] Z. Warhaft, Annual Review of Fluid Mechanics **32**, 203 (2000), <https://doi.org/10.1146/annurev.fluid.32.1.203>.
  - [16] G. Katul, A. Porporato, D. Cava, and M. Siqueira, Physica D: Nonlinear Phenomena **215**, 117 (2006).
  - [17] J. L. Lumley (Elsevier, 1979) pp. 123 – 176.
  - [18] S. Banerjee, R. Krahl, F. Durst, and C. Zenger, Journal of Turbulence **8**, N32 (2007), <https://doi.org/10.1080/14685240701506896>.
  - [19] T. Foken, R. Leuning, S. R. Oncley, M. Mauder, and M. Aubinet, in *Eddy Covariance A Practical Guide to Measurement and Data Analysis*, edited by D. P. Marc Aubinet, Timo Vesala (Springer Netherlands, 2012) Chap. 4, pp. 85–125.
  - [20] A. Kolmogorov, Akademiia Nauk SSSR Doklady **30**, 301 (1941).
  - [21] U. Frisch, *Turbulence: The Legacy of A. N. Kolmogorov* (Cambridge University Press, 1995).
  - [22] M. Ghil, R. Benzi, and G. Parisi, eds., *Turbulence and Predictability in Geophysical Fluid Dynamics and Climate Dynamics* (North-Holland Publ. Co., Amsterdam/New York, 1985) p. 449.
  - [23] R. Benzi, G. Paladin, G. Parisi, and A. Vulpiani, Journal of Physics A: Mathematical and General **17**, 3521 (1984).
  - [24] T. C. Halsey, M. H. Jensen, L. P. Kadanoff, I. Procaccia, and B. I. Shraiman, Phys. Rev. A **33**, 1141 (1986).
  - [25] F. Argoul, A. Arneodo, G. Grasseau, Y. Gagne, E. J. Hopfinger, and U. Frisch, Nature **338**, 51 (1989).
  - [26] C. Meneveau and K. R. Sreenivasan, Journal of Fluid Mechanics **224**, 429–484 (1991).
  - [27] G. Boffetta, A. Mazzino, and A. Vulpiani, Journal of Physics A: Mathematical and Theoretical **41**, 363001 (2008).

- [28] R. Smalley, S. Leonardi, R. Antonia, L. Djenidi, and P. Orlandi, *Experiments in Fluids* **33**, 31 (2002).
- [29] H. Liu, R. Yuan, J. Mei, J. Sun, Q. Liu, and Y. Wang, *Boundary-Layer Meteorology* **165**, 277 (2017).
- [30] S. Sarkar and C. G. Speziale, *Physics of Fluids A: Fluid Dynamics* **2**, 84 (1990), <https://doi.org/10.1063/1.857694>.
- [31] J. P. Panda, H. V. Warrior, S. Maity, A. Mitra, and K. Sasmal, *Journal of Fluids Engineering* **139** (2017), 10.1115/1.4035467, 044503.
- [32] F. G. Schmitt, *Communications in Nonlinear Science and Numerical Simulation* **12**, 1251 (2007).
- [33] J. L. Lumley and G. R. Newman, *Journal of Fluid Mechanics* **82** (1977), 10.1017/S0022112077000585.
- [34] R. A. Antonia, J. Kim, and L. W. B. Browne, *Journal of Fluid Mechanics* **233** (1991), 10.1017/S0022112091000526.
- [35] P.-A. Krogstad and L. E. Torbergsen, *Flow, Turbulence and Combustion* **64**, 161 (2000).
- [36] G. Katul, B. Vidakovic, and J. Albertson, *Physics of Fluids* **13**, 241 (2001), <https://doi.org/10.1063/1.1324706>.
- [37] G. G. Katul, A. Porporato, and D. Poggi, *Physics of Fluids* **21**, 035106 (2009), <https://doi.org/10.1063/1.3097005>.
- [38] B. Shi, B. Vidakovic, G. G. Katul, and J. D. Albertson, *Physics of Fluids* **17**, 055104 (2005).
- [39] A. Arnèodo, R. Benzi, J. Berg, L. Biferale, E. Bodenschatz, A. Busse, E. Calzavarini, B. Castaing, M. Cencini, L. Chevillard, R. T. Fisher, R. Grauer, H. Homann, D. Lamb, A. S. Lanotte, E. Lévêque, B. Lüthi, J. Mann, N. Mordant, W.-C. Müller, S. Ott, N. T. Ouellette, J.-F. Pinton, S. B. Pope, S. G. Roux, F. Toschi, H. Xu, and P. K. Yeung (International Collaboration for Turbulence Research), *Phys. Rev. Lett.* **100**, 254504 (2008).
- [40] S. S. Ray, D. Mitra, and R. Pandit, *New Journal of Physics* **10**, 033003 (2008).
- [41] R. Pandit, P. Perlekar, and S. S. Ray, *Pramana - J Phys* **224** (2009), 10.1007/s12043-009-0096-6.
- [42] N. Pal, P. Perlekar, A. Gupta, and R. Pandit, *Phys. Rev. E* **93**, 063115 (2016).
- [43] M. Zeng, X.-N. Zhang, J.-h. Li, and Q.-h. Meng, *ACTA Physica Polonica B* **47**, 2205 (2016).
- [44] S. Buldyrev, N. Dokholyan, A. Goldberger, S. Havlin, C.-K. Peng, H. Stanley, and G. Viswanathan, *Physica A: Statistical Mechanics and its Applications* **249**, 430 (1998).
- [45] J. J. Z. J. Gieraltowski and R. Baranowski, *Physical Review E* **021915**, 1 (2012).
- [46] P. C. Ivanov, A. N. Amaral, and H. E. Stanley, *Nature* **399**, 461 (1999).
- [47] K. Ivanova, M. Ausloos, E. E. Clothiaux, and T. P. Ackerman, *Europhysics Letters (EPL)* **52**, 40 (2000).
- [48] R. N. Mantegna and H. E. Stanley, “An introduction to econophysics: correlations and complexity in finance,” (1999).
- [49] K. R. Amin, S. S. Ray, N. Pal, R. Pandit, and A. Bid, *Communications Physics* **1**, 1 (2018).
- [50] J. Sutradhar, S. Mukerjee, R. Pandit, and S. Banerjee, *Phys. Rev. B* **99**, 224204 (2019).
- [51] E. A. F. Ihlen, *Frontiers in Physiology* **3**, 1 (2012).
- [52] J. W. Kantelhardt, S. A. Zschiegner, E. Koscielny-bunde, S. Havlin, A. Bunde, and H. E. Stanley, *Physica A* **316**, 87 (2002).
- [53] G. G. Katul, A. Porporato, C. Manes, and C. Meneveau, *Physics of Fluids* **25**, 091702 (2013).
- [54] G. G. Katul, A. Porporato, S. Shah, and E. Bou-Zeid, *Physical Review E* **89**, 023007 (2014).
- [55] S. G. Saddoughi and S. V. Veeravalli, *Journal of Fluid Mechanics* **268**, 333–372 (1994).
- [56] D. Cava and G. G. Katul, *Boundary-Layer Meteorology* **145**, 351 (2012).
- [57] P. A. Davidson, T. B. Nickels, and P.-A. Krogstad, *Journal of Fluid Mechanics* **550**, 51–60 (2006).
- [58] C.-I. Hsieh and G. G. Katul, *Journal of Geophysical Research: Atmospheres* **102**, 16391 (1997).
- [59] D. Cava and G. G. Katul, *Boundary-Layer Meteorology* **130** (2009), 10.1007/s10546-008-9342-6.
- [60] K. R. Sreenivasan and A. Bershadskii, *Journal of Statistical Physics* **125**, 1141–1153 (2006).
- [61] C. Meneveau and K. Sreenivasan, *Nuclear Physics B - Proceedings Supplements* **2**, 49 (1987).
- [62] Z.-S. She and E. Leveque, *Phys. Rev. Lett.* **72**, 336 (1994).
- [63] R. Benzi, S. Ciliberto, R. Tripiccone, C. Baudet, F. Massaioli, and S. Succi, *Phys. Rev. E* **48**, R29 (1993).
- [64] S. Chakraborty, U. Frisch, and S. S. Ray, (2009), [arXiv:0912.2406 \[nlin.CD\]](https://arxiv.org/abs/0912.2406).
- [65] I. Arad, L. Biferale, I. Mazzitelli, and I. Procaccia, *Phys. Rev. Lett.* **82**, 5040 (1999).
- [66] L. Biferale and I. Procaccia, *Physics Reports* **414**, 43 (2005).
- [67] See the movie in supplementary materials.
- [68] R. Campbell, (2020).